

DISS. ETH No. 22191

**FINITE ELEMENT
SIMULATIONS AND OPTIMIZATIONS OF
PLASMONIC STRUCTURES IN LAYERED MEDIA**

A dissertation submitted to the

ETH ZÜRICH

for the degree of
Doctor of Sciences

presented by
MENGYU WANG

B.S. in Electrical and Electronics Engineering
M.S. in Electrical and Computer Engineering
Zhejiang University, Hangzhou, China

born June 20, 1983

citizen of China

accepted on the recommendation of

Prof. Dr. Ch. Hafner, examiner
Prof. Dr. R. Hiptmair, co-examiner
Dr. Ch., Engström co-examiner

2014

DISS. ETH No. 22191

**FINITE ELEMENT
SIMULATIONS AND OPTIMIZATIONS OF
PLASMONIC STRUCTURES IN LAYERED MEDIA**

A dissertation submitted to the

ETH ZÜRICH

for the degree of
Doctor of Sciences

presented by

MENGYU WANG

B.S. in Electrical and Electronics Engineering

M.S. in Electrical and Computer Engineering

Zhejiang University, Hangzhou, China

born June 20, 1983

citizen of China

accepted on the recommendation of

Prof. Dr. Ch. Hafner, examiner

Prof. Dr. R. Hiptmair, co-examiner

Dr. Ch., Engström co-examiner

2014

Abstract

This thesis focuses on the finite element modeling and optimization of plasmonic structures in layered media. In plasmonics, the lossy and dispersive nature of metals causes special effects, such as surface plasmon resonances and strong local field enhancement. These effects cause many challenges for the numerical solvers, namely rapid field variation and field singularities. Layered media need additional effects, *e. g.*, guided waves. Plasmonic objects embedded in layered media can be utilized as optical antennas, sensors, and couplers, which are of great value in many applications of plasmonics. However, layered media also lead several challenges to numerical solvers. The layers are assumed to extend to infinity. Therefore the computational domain must be properly truncated. Moreover, layered structures lead to more complicated field distributions than standard free space scattering.

We first consider the advantages and disadvantages of many classes of numerical solvers with respect to plasmonic effects. This thesis focuses on the finite element implementation in the frequency domain, which is considered to be most appropriate for complicated plasmonic configurations. After comparing many candidates, the high order curvilinear finite element package **CONCEPTs** is chosen.

Absorbing boundary conditions (ABCs) are formulated to study open scattering problems. Then the Bayliss-Gunzburger-Turkel (BGT) conditions are implemented in **CONCEPTs**. The BGT conditions of different orders are studied and compared. Moreover, the perfectly matched layers (PMLs) are formulated to study the plasmonic structures in layered media. Then Cartesian PML is implemented in **CONCEPTs**. *hp*-FEM analyses are performed thoroughly to study the behavior of PML. Based on them, an *hp*-strategy is proposed and applied.

Another part of the thesis is on the optimization of the plasmonics structures. Unlike the traditional radio frequency (RF) applications, plasmonic devices may resonate even if they are much smaller than the wavelength. Therefore, the design of plasmonic devices is much more demanding. A framework of a combination of numerical optimizers with numerical field solvers is implemented. As an example, we study two versions of ultra short two-dimensional plasmonic waveguide couplers. The program optimizes the problem using an evolution strategy (ES). Finally, optimized geometries are obtained. For the simpler version of the waveguide coupler, the multiple multipole program (MMP) solution is used for a comparison as well.

Zusammenfassung

Diese Dissertation befasst sich mit der Finite Elemente Modellierung und der Optimierung von plasmonischen Strukturen in mehrschichtigen Anordnungen. In der Plasmonik führen Verluste und Dispersion von Metallen zu speziellen Effekten wie Resonanzen von Oberflächenplasmonen und starken lokalen Feldüberhöhungen. Diese Effekte führen zu mehreren Herausforderungen für numerische Feldberechnungsverfahren, namentlich rasche Feldänderungen und Feldsingularitäten.

Mehrschichtstrukturen führen zu weiteren Effekten wie geführten Wellen. Plasmonische Objekte, welche in Mehrschichtstrukturen eingebettet sind können als optische Antennen, Sensoren und Koppler ausgenutzt werden. Diese sind für diverse Anwendungen von grossem Wert. Mehrschichtstrukturen bringen aber auch einige Herausforderungen für numerische Verfahren mit sich. Weil die Schichten als unendlich ausgedehnt betrachtet werden, muss das Deltdgebiet für die Berechnungen passend begrenzt werden. Darüber hinaus führen Mehrschichtstrukturen zu komplizierteren Feldverteilungen als gewöhnlich Streuung an Objekten im Freiraum.

Zu Beginn werden die Vor- und Nachteile verschiedener Klassen numerischer Methoden in Bezug auf plasmonische Effekte betrachtet. Anschliessend wird auf die Finite Elemente Methode (FEM) im Frequenzbereich fokussiert, da diese als besonders aussichtsreich für komplizierte plasmonisch Strukturen erachtet wird. Nach dem Vergleich vieler FEM Kandidaten wird **CONCEPTs** ausgewählt, da dieses mit gekrümmten Elementen hoher Ordnungen arbeiten kann.

Um offene Streufeldprobleme behandeln zu können werden absorbierende Randbedingungen studiert. Anschliessend werden die Bayliss-Gunzburger-Turkel (BGT) Bedingungen in **CONCEPTs** implementiert. Unterschiedliche BGT Ordnungen werden untersucht und verglichen. Darüber hinaus werden perfectly matched layers (PML) untersucht um plasmonische Strukturen in Mehrschichtstrukturen analysieren zu können. Anschliessend werden Kartesische PML in **CONCEPTs** implementiert. Sorgfältige hp-FEM Untersuchungen werden durchgeführt um das PML Verhalten zu bestimmen. Darauf basierend wird eine hp-Strategie vorgeschlagen und angewendet.

Ein weiterer Teil der Dissertation untersucht die Optimierung plasmonischer Strukturen. Anders als bei traditionellen Radiofrequenzanwendungen weisen plasmonische Objekte auch dann Resonanzen auf, wenn sie viel kleiner als die Wellenlänge sind. Das macht das Design plasmonischer Strukturen sehr anspruchsvoll. Eine passende Kombination numerischer Optimierungsverfahren mit Feldberechnungsmethoden wird erarbeitet. Als Beispiele werden zwei Versionen ultra-kurzer plasmonischer Koppler optimiert, wobei eine 'evolution strate-

gy' (ES) zur Anwendung kommt. Auf diese Weise werden optimierte Geometrien gefunden. Für die einfachere Kopplerversion wird auch eine MMP Lösung zum Vergleich herangezogen.

Contents

List of Publications	XXI
1 Introduction	1
1.1 Outline of the thesis	2
2 Numerical methods for plasmonics	3
2.1 Introduction	3
2.2 Selection of the solvers	3
2.2.1 Time and frequency domain	3
2.2.2 Boundary and domain discretization methods	5
2.2.3 Structured and unstructured meshes	8
2.3 Selection of elements	9
2.4 CONCEPTs	12
3 Truncation techniques	13
3.1 Introduction	13
3.2 Absorbing Boundary Conditions (ABC)	13
3.2.1 Scattering problem and BGT conditions	14
3.2.2 Finite elements formulation and discretization	14
3.2.3 Numerical results and discussions	20
Scattering from one cylinder	20
Scattering from two cylinders	25
3.3 Perfectly Matched Layers (PML)	31
3.3.1 Finite element formulation and implementation	32
Finite element variational formulation using PML	32
CONCEPTs implementation	35
3.3.2 Numerical simulations	37
3.3.3 <i>hp</i> -FEM analysis	41
3.4 Summary	47
4 Numerical optimizations	49
4.1 Introduction	49
4.2 Numerical optimizers	50
4.3 Test problems	52
4.4 Solvers for plasmonic structures	55
4.5 Simulation methods	56

4.5.1	Boundary discretization - MMP	56
4.5.2	Domain discretization - FEM/CONCEPTs	56
4.6	Optimization results	59
4.6.1	The first test problem	59
	Deterministic optimization with COMSOL	62
4.6.2	The second test problem	63
4.7	Summary	66
5	Conclusion	69
5.1	Summary	69
5.2	Outlook	70
A	Dielectric scattering formulation and implementation	71
	Bibliography	77
	Curriculum Vitae	89

List of Figures

2.1	The dispersive relationship of silver at optical frequencies. The solid lines represent data computed from the Drude model, while the dashed lines represent measurement data from Palik and Johnson & Christy, respectively. (a) the real part, (b) the imaginary part.	6
2.2	Comparison of straight and curved elements. The dots are quadrature points on one edge. The curved lines in a) and b) represent the real boundaries of the objects. a) straight element of order 1. b) straight element of order 4. c) curved element of order 4. . . .	10
2.3	Mapping from the reference elements. F represents the mapping. a) mapping from the reference triangle. b) mapping from the reference square.	11
3.1	Computational domain Ω with the region of the scatter Ω_ϵ and artificial circular boundary Γ_0	16
3.2	CONCEPTs mesh with 13 curved quadrilateral cells used in the p -FEM computations with CONCEPTs.	17
3.3	Example of triangular mesh generated by FreeFEM++.	18
3.4	The absolute value of total magnetic field, with 2596 degree of freedom. The radius of the silver wire is 400nm, and the wavelength is 413nm. The permittivity of silver $-5.0092942+0.2194588i$, is calculated from the Drude model (3.9). A strong surface plasmon resonance is observed.	19
3.5	The comparison of $ \mathbf{H}^{\text{total}} $ across the material interface, between CONCEPTs results and MMP results. The mesh is shown in figure 3.2 with the degrees of freedom 2956, and the absorbing boundary is 2λ away from the scatterer.	21
3.6	p -FEM convergence. The distance between the boundary and the scatterer is 1,2,4,6, and 8 times of the wavelength, respectively.	22
3.7	A finer mesh and the solution. This mesh, consisting of 52 elements, is obtained after one step of uniform h -refinement based on the mesh in Figure 3.2.	23
3.8	The relationship between computation time and relative L^2 error from scattering of one cylinder: (a) with the mesh shown in Figure 3.2, and (b) with the finer mesh in Figure 3.7.	24

3.9	The CONCEPTs mesh of the two cylinders computation example. The mesh consists of 52 cells.	26
3.10	The absolute value of total magnetic field. The radius of the silver wire is 400nm and the gap between the two wires is 20nm, with incoming wave of wavelength 413nm. A strong local enhancement can be observed in the gap area.	27
3.11	Comparison between MMP and CONCEPTs results of $ H^{\text{total}} $ in the two cylinder case, the values are taken across the the material interface of the upper cylinder. The absorbing boundary is 4λ away from the scatterer, and the computation consumes 13409 degrees of freedom.	28
3.12	Convergence for the two cylinders case. The solid lines represent the p -convergence for the boundary $1,2,4$, and 6λ away from the scatterer, respectively. The dashed line represents the h -convergence for the boundary 4λ away from the scatterer, using quadratic curvilinear finite elements. A and B are two selected computation examples in Figure 3.13.	28
3.13	The structure of the system matrices: (a) for test example A in Figure 3.12, (b) for test example B in Figure 3.12.	30
3.14	Scattering from the multi-layered test structure, illuminated by a plane wave from top. Scattered and guided waves can be excited. The physical domain is surrounded by a PML.	34
3.15	CONCEPTs and COMSOL meshes near the scatterer. (a) The CONCEPTs mesh using quadrilateral elements generated by EZ4U. (b) The COMSOL mesh using triangular elements.	36
3.16	Simulation results for the absolute value of the total magnetic field. In (a),(c) and (e) the results for circular scatterer are shown, and (b),(d) and (f) the results for triangular scatterer. The results with CONCEPTs are in (a),(b), where we use a polynomial degree of 14 resulting in 22741 DOFs for the disk, and 21876 DOFs for the triangle. (c),(d) show the MMP results. For the disk, 64 layered expansions and a Bessel expansion with the maximum order of 30 are used. For the triangle, 51 multilayer expansions are used inside the scatterer and 23 homogeneous media multipoles are used outside the scatter. (e),(f) COMSOL results using quadratic elements, where 155798 DOFs are used for the disk and 177477 DOFs for the triangle.	38

3.17 Comparisons for the normalized absolute value of the total magnetic field along the trace of the silver disk Γ (in logarithmic scale). The red curve represents the MMP result. The black dots represent the **CONCEPTs** result. The black dashed curve represents the difference between **CONCEPTs** and MMP results; the blue dashed curve represents the difference between MMP result and **COMSOL** result using quadratic elements, and the red dashed curve represents the difference between MMP result and **COMSOL** result using cubic elements. 40

3.18 Adaptive h -refinement. (a) the original mesh h_0 . (b) mesh h_1 , obtained by one step of h -refinement from mesh h_0 . (c) mesh h_2 , obtained by one more step of h -refinement from mesh h_1 42

3.19 The hp -convergence analysis for the scattering problem of a silver disk. Each node represents a simulation with an hp combination of $(p_{\text{int}}, p_{\text{ext}}, \ell)$. (a) A group of 20 simulations with $p_{\text{int}} = 8$, $p_{\text{ext}} \in [4, 6, 8, 10]$, and $\ell \in [0, 1, 2, 3, 4]$, (b) A group of simulations with $p_{\text{int}} = 10$, $p_{\text{ext}} \in [6, 8, 10, 12]$, and $\ell \in [0, 1, 2, 3, 4]$. The solid lines connect the nodes with the same mesh and show the convergence with respect to p_{ext} . And the dashed lines connect the nodes with the same p_{ext} and show the convergence with respect to the mesh refinement. 43

3.20 The hp -convergence strategy. Three options are represented by a,b, and c, where a means increasing p_{int} by 2, b means increasing p_{ext} by 2, and c means increasing ℓ by 1. The experiment starts at the hp combination (8,6,0) with 5979 DOFs and an error of 4.05×10^{-1} , and stops at the hp combination (10,6,4) with 15389 DOFs and an error of 2.83×10^{-6} 46

4.1 The geometrical configuration of the test problem. The dielectric waveguide with permittivity 4.0 is placed in between the glass and air. Two silver cylinders are embedded in the waveguide. The structure is excited by an H_z polarized plane wave with 600 nm wavelength. The location of the cylinders is characterized by $\bar{V} = \{v_1, v_2, v_3, v_4, v_5\}$, which are the parameters of the optimization problem. 52

4.2 The geometrical configuration of the second test problem. The dielectric waveguide with permittivity 4.0 is placed in between the glass and air. Two silver rods are placed on the surface of the waveguide. The structure is excited by an H_z polarized plane wave with 600 nm wavelength. The location of the rods is characterized by l, h, d , which are the parameters of the optimization problem. 54

-
- 4.3 The control flow of the optimization. The framework of parametric mesh generation links **CONCEPTs** with **COMSOL**. 56
- 4.4 **COMSOL** mesh with mixed quadrilateral and triangular elements, which causes problems when solving with **CONCEPTs**. The red circle points out the problematic triangular elements. This problem can be solved by increasing the overall refinement level. 57
- 4.5 **COMSOL** elements with neighboring curved edges, which causes problems when solving with **CONCEPTs**. The red circle points out one of the problematic elements. This problem can be solved by a further refinement of the circular interface. Note that in the illustration, straight-sided elements are displayed as generated by **COMSOL**. Problems occur only when the elements are subsequently curved leading to coordinate degeneration at the node indicated by the arrow. 57
- 4.6 The results of the 5-dimensional optimization. The maximum number of individual simulations is 1000, with the number of parents $\mu = 5$, number of children $\lambda = 35$, and strength of mutation $\sigma = 0.1$. p_1 to p_5 are the normalized geometrical parameters, which are mentioned in section 4.3. The strategy keeps the best 5 parent individuals in each generation.(a) shows the convergence with respect to the number of iterations using MMP, and (b) shows the distribution of the normalized parameters versus the fitness function using MMP. (c),(d) are the corresponding results from the first run of **CONCEPTs** simulation, and (e),(f) are from the second run of **CONCEPTs** simulation. The optimizations look different each time, only due to the randomness of the optimizer. 61
- 4.7 Five-dimensional optimization using Nelder-Mead method in **COMSOL**. There are 172 instances of simulations, with optimality tolerance of 0.01 and the initial values of the optimization set to be the mid-point of the corresponding parameter bounds. p_1 to p_5 are the normalized geometrical parameters, which are mentioned in section 4.3. The figure shows the distribution of the parameters versus the fitness function. 63
- 4.8 The fitness function of a two-dimensional scan using OpenMaXwell. The scanning parameters are the distance between the two cylinders v_3 , and the lower distance from the substrate v_0 , respectively. 63

4.9	The results of the optimization with the strength of mutation $\sigma = 0.1$. The maximum number of individual simulations is 600, with the number of parents $\mu = 5$, number of children $\lambda = 35$. p_1 to p_3 are the normalized geometrical parameters, which are mentioned in section 4.3. The strategy keeps the best 5 parent individuals in each generation. (a) shows the convergence with respect to the number of iterations, and (b) shows the distribution of the normalized parameters versus the fitness function. The maximum fitness only reaches 0.54, since the optimization failed to find the global optimum.	64
4.10	The results of the scan of the three optimization parameters. The scans are performed with the other two parameters set to the values of the global optimum. (a) shows the scan of l , (b) shows the scan of d , and (c) shows the scan of h . One can observe that the scan of d has a very sharp peak at the global optimum between 200 and 400 nm.	65
4.11	The results of the optimization with the variation parameter $\sigma = 0.2$. The maximum number of individual simulations is 600, the number of parents $\mu = 5$, and the number of children $\lambda = 35$. p_1 to p_3 are the normalized geometrical parameters, which are mentioned in section 4.3. The ES keeps the best 5 parent individuals in each generation. (a) shows the convergence with respect to the number of iterations, and (b) shows the distribution of the normalized parameters versus the fitness function. The maximum normalized fitness reaches 1.0, which corresponds to the global optimum.	66
A.1	The computation domain of dielectric scattering problem.	71

List of Tables

3.1	The coefficients of the BGT absorbing boundary conditions in (3.2)	15
3.2	The implementation of the integrals in CONCEPTs	36
A.1	The coefficients of BGT absorbing boundary conditions	72
A.2	The implementation of the integral in CONCEPTs	75

List of Acronyms and Abbreviations

1D	one dimensional
2D	two dimensional
3D	three dimensional
ABC	absorbing boundary condition
BEM	boundary element method
BGT	Bayliss-Gunzburger-Turkel (condition)
CAD	computer-aided design
DG	discontious Galerkin
DOF	degree of freedom
EM	electromagnetic
ES	evolution strategy
FD	frequency domain
FDTD	finite difference time domain
FDM	finite difference method
FEM	finite element method
FVTD	finite volume time domain
GA	genetic algorithm
GUI	graphical user interface
MMP	multiple multipole program
MoM	method of moments
PML	perfectly matched layer
RF	radio frequency

SPP	surface plasmon polariton
TD	time domain
TE	transverse electric
TM	transverse magnetic

List of Publications

Journal papers related to this thesis

- P1** M. Wang, Ch. Engström, K. Schmidt and Ch. Hafner, “On high-order FEM applied to canonical scattering problems in plasmonics”, *Journal of Computational and Theoretical Nanoscience*, Vol. 8, pp.1564–1572, 2011.
- P2** M. Wang, K. Schmidt, A. Alparslan, and Ch. Hafner, “Hp-FEM and PML analysis of plasmonic particles in layered media”, *Progress In Electromagnetics Research*, Vol. 142, pp. 523–544, 2013.
- P3** M. Wang, A. Alparslan, S. Schnepf, and Ch. Hafner, “Optimization of a Plasmon-Assisted Waveguide Coupler Using FEM and MMP”, *Progress In Electromagnetics Research B*, Vol. 59, pp. 219–229, 2014.

Journal papers not related to this thesis

- P4** Ch. Engström, M. Wang, “Complex dispersion relation calculations with the symmetric interior penalty method”, *International Journal for Numerical Methods in Engineering*, Vol. 84, pp.849–863, 2010.

1 Introduction

Advancing fabrication techniques in Nano-technology made it more and more popular to study structures in the size of optical wavelengths or even less. There are many applications, such as nano antennas [1, 2], photonic crystals [3], and chemical and biological sensors [4, 5, 6]. However, the rapid development of plasmonic devices brings challenges to the engineers. For example, radio frequency (RF) antennas are often surrounded by air and their holders have almost no impact on the performance, while optical antennas are usually mounted on or embedded in layered media. Due to the surface plasmon polaritons (SPP), leaky waves, etc., the underlying substrate can strongly affect the performance of optical antennas and its influence cannot be ignored.

In early times of RF design, a pure analytical approach could be applied. Later, many empirical formulae became available to assist RF engineering. Nowadays, with the rapid growth of the complexity of the devices, RF design relies more and more on simulations. In the design of plasmonic devices, the first two approaches are very difficult or even not feasible at all. Firstly, there are many design variables, *e. g.*, the geometrical parameters and material parameters, and even small changes in some of the design variables may have a strong impact on the performance of the devices. Secondly, plasmonic structures are not scalable, *i. e.*, a complete redesign may be needed for changing the operation frequency. Due to the high complexity of the problem, the analytical approach is nearly impossible, and even the empirical formulae are of very limited value. Therefore, simulation and numerical optimizations are indispensable for the design of the plasmonic devices.

In recent decades, computer science and computer-aided design (CAD) technology made rapid progress. They provide an easy access to numerical simulations to engineers in all fields. The growing power of computers brings the possibility to study large and complicated problems.

Due to the high sensitivity with respect to several design parameters, simulation tools need to be accurate. Since the computational cost grows strongly with the problem complexity, the simulation tools must also be efficient, *i. e.*, high performance solvers are important for the design. Here, high-order finite element method (FEM) obviously is a promising candidate.

1.1 Outline of the thesis

In Chapter 2, various numerical methods for plasmonics are discussed. The finite element method (FEM) is selected and comparisons are performed with other methods, such as, Finite difference time domain method (FDTD), boundary element method (BEM). In this thesis, the high order hp-FEM package **CONCEPTs** is exploited. An introduction to **CONCEPTs** is also given in this chapter.

In chapter 3, truncation techniques for the simulation of plasmonics are discussed. In this thesis, an absorbing boundary condition (ABC) for free space and a perfectly matched layer (PML) for infinite waveguides and substrates are implemented. Plasmonic cylinders are studied as test problem for the ABC, and plasmonic scatterers in a dielectric waveguide are considered as test problem for the PML. Convergence studies are made to analyze the behavior of these absorbers. Some comparisons with other solvers show the advantage of high order FEM. The **CONCEPTs** implementation is also introduced. This chapter is essentially published in [7, 8].

In chapter 4, we focus on the optimal design of plasmonic waveguide couplers. We combine an evolution strategy (ES) optimizer with a high order FEM solver. The framework of the optimizer is described. A robustness study of the optimizer is made and many issues are discussed. Two test examples are studied and optimal structures are proposed. This chapter is essentially published in [9].

2 Numerical methods for plasmonics

2.1 Introduction

In this chapter, we discuss the selection of the numerical methods for plasmonics. Plasmonics has dispersive and lossy properties in the optical frequency range. Moreover, there are special effects, such as surface plasmon resonances [10], which can lead to rapid local field variation. In order to obtain reliable results, we need to choose the method carefully.

Currently, there are many numerical methods available, and there are various criteria of categorization. One way to categorize the solvers is to distinguish time and frequency domain. Another one is to distinguish boundary and domain discretization. In domain discretization methods, one can further categorize the solvers by the mesh structures. One class contains structured meshes, which are used, for example, in the finite difference time domain (FDTD) method [11], while the other one contains unstructured meshes, which are used, for example, in the finite element method (FEM) [12].

Furthermore, there are issues concerning the selection of elements in the FEM solvers. One can choose between high and low order elements, curvilinear and straight elements, and triangular and quadrilateral elements. In plasmonics, one can indeed benefit from high order, curvilinear elements.

In this and the following chapter, we show that frequency domain FEM with high order curved elements is well suited for plasmonics. We therefore select `CONCEPTs`, which is an open source c++ FEM library [13, 14, 15, 16], that uses high order, curvilinear, quadrilateral elements. More importantly, `CONCEPTs` can support *hp*-FEM adaptation. In order to validate the results, we use the multiple multipole program (MMP), a frequency domain, boundary discretization technique contained in the open source package OpenMaXwell [17, 18, 19, 20, 21].

2.2 Selection of the solvers

2.2.1 Time and frequency domain

Time domain

Solvers in the time domain (TD) [22] solve Maxwell equations by discretized time steps. TD solvers have several advantages, *e. g.*, they can study the whole spectrum in one simulation, and they can analyze transient signals and configurations with non-linear materials. However, the disadvantages of the TD solvers

are more important in plasmonics. Severe difficulties occur if strongly dispersive material are present. Furthermore, extremely many time steps are needed to converge when strong resonances occur. Interestingly, one observes field singularities in plasmonics not only near tips (lightning rod effect) and sharp corners but also in grooves. This leads to severe staircasing effects in FDTD. As a result extremely fine meshes are required.

Currently, the FDTD method is one of the most well-known and most widely applied techniques[11]. FDTD solves the coupled Maxwell equations usually with a leapfrog scheme, which is called Yee scheme [23].

It is also possible to apply FEM [12] in TD. However, the cost is too high in standard FEM, since the local change of each element will influence the global matrices. In order to separate the local changes from the global matrices, numerical fluxes were introduced [24]. With numerical fluxes, a local change in one element will directly affects its neighbors as in FDTD. Therefore, only a small local matrix is updated for each element in each time step. Moreover, numerical fluxes are valuable to couple different methods on the boundaries. This method was first used in the finite volume time domain (FVTD) method [25]. As a more generalized version of FVTD, the discontinuous Galerkin (DG)method [24] became very popular recently. FVTD uses central fluxes, which are included as a special case of the generalized numerical fluxes in DG. DG also uses internal penalty fluxes [24] to restrict the jump terms between the elements. Moreover, it supports high order, curvilinear elements, and therefore it is very flexible. DG is certainly a promising candidate for future TD solvers.

Frequency domain

Frequency domain (FD) solvers work with the Maxwell equations in the frequency domain. The fields are then expressed by harmonic components. FD is very efficient when the source has single frequency or a discrete spectrum. Furthermore, FD gives stationary solutions directly. However, FD solvers also have disadvantages. They depict the stationary solutions, but require Fourier analysis for obtaining transient signals. Moreover, FD solvers have severe problems with non-linear materials.

TD solvers, such as Finite Differences, FEM and DG, also have representatives in FD. FEM in FD is one of the most commonly-used solvers [12]. FEM uses variational formulations to solve boundary value problems of differential equations. The finite difference method (FDM) uses finite difference equations to approximate derivatives [26]. Moreover, many boundary element method (BEM) solvers work in FD. Note that many FD solvers have severe problems in TD (*e.g.* method of moments (MoM)) or were never implemented in TD (*e.g.* MMP).

For plasmonics

In plasmonics, metals are indeed dispersive and lossy. TD solvers then need appropriate simplified models for reducing the numerical costs for solving convolution integrals. For example, in the optical frequency range, silver can be approximated by the Drude model [27, 28]. Figure 2.1 shows its dispersive behavior, the solid line is from the Drude model, while the dashed lines are from the measurement data of Palik [29] and Johnson & Christy [30], respectively.

Firstly, one can see that the Drude model is only a rough approximation of the permittivity within a limited spectrum. A better approximation is the Drude–Lorentz model [27], with higher order approximations. Secondly, due to different sample preparation methods, the two sets of measurement data are rather different. Therefore, sample preparation is crucial in plasmonics. Finally, one can also see that the spectra are complicated.

As a result, no TD solver can provide accurate results with low computational costs. In this thesis, we will study silver scatterers without any nonlinear materials at optical frequencies. Therefore, we focus on FD solvers in the following.

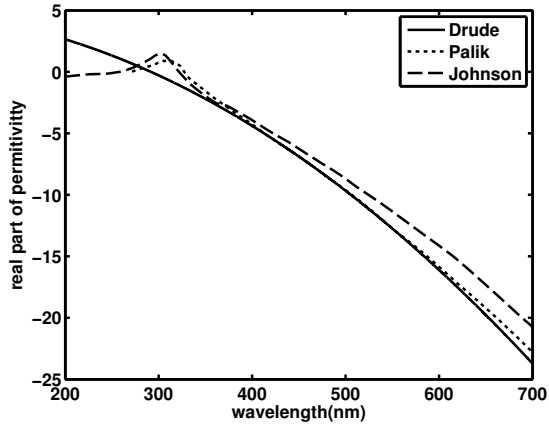
2.2.2 Boundary and domain discretization methods

Another way to categorize solvers is to distinguish between boundary discretization methods and domain discretization methods.

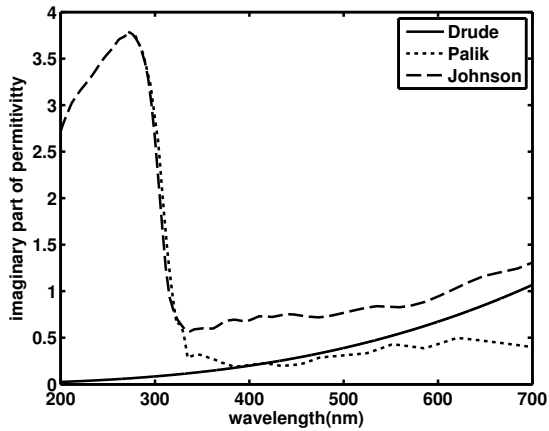
Boundary discretization methods

Boundary discretization methods approximate the fields in domains by superpositions of fundamental solutions that fulfill the field equations analytically. These methods are usually good for studying simple and smooth geometries. They reduce the discretization space by one dimension, *i. e.*, 2D instead of 3D, or 1D instead of 2D. Therefore, they work with a small number of elements, and degrees of freedom (DOFs) are rather low. However, this leads to dense and often ill-conditioned matrices. Boundary discretization methods do not work very efficiently when solving complicated structures, especially when sharp corners and triple points are present. Moreover, boundary discretization methods is confined to homogeneous materials.

One of the most important solvers is the boundary element method (BEM). BEM uses Green’s functions as the basis functions [31]. In electromagnetics, Green’s functions are also used in the method of moments (MoM) and other techniques. A more generalized solver is the multiple multipole program (MMP). It is based on the separation of variables to find appropriate basis functions, such as multipoles of arbitrary orders, harmonic functions, Green’s functions, etc [17, 18, 19, 20].



(a)



(b)

Figure 2.1: The dispersive relationship of silver at optical frequencies. The solid lines represent data computed from the Drude model, while the dashed lines represent measurement data from Palik and Johnson & Christy, respectively. (a) the real part, (b) the imaginary part.

Domain discretization methods

Domain discretization methods discretize the whole geometry of the objects and of the surroundings. Therefore the DOFs are high, but the matrices are usually very sparse and well-conditioned. Domain discretization methods can represent complicated objects rather precisely, especially when curvilinear elements are used. In contrast to boundary discretization methods, they usually consume more memory.

There are many important members of domain discretization methods. FEM, DG, and FVTD work on sets of elements that discretize the computational domain. FDTD solves differential equations on grids that discretize the domain of interest. Recently, a new kind of domain discretization solver was developed - the meshless method [32], which does not use traditional mesh structures, but discretizes the geometry through collocation nodes. Note that MMP can be considered as a meshless boundary discretization method.

An important issue is the truncation of the computational domain. In boundary discretization methods, their basis functions are naturally global. Therefore, no truncation is needed at least as long as none of the boundaries extends to infinity. For domain discretization methods, the computational domain must be truncated if it extends to infinity, which is the case for most of the practical problems and especially for antenna and scattering problems. Many numerical issues on truncation techniques have been studied. This will be addressed in detail in chapter 3.

For plasmonics

In this thesis, we will focus on domain discretization, in order to be able to also work for geometrically complicated structures and complicated materials. In order to evaluate the accuracy of our solver, we first consider simple and smooth geometries as the problems. Since the accuracy of our solver is higher than that of available commercial softwares, we need reliable reference solutions with high accuracy. Some very simple problems, such as single particle scattering in the free space, have analytical solutions [33], and therefore can be used as reference with arbitrary digits of accuracy. However, we study other problems, such as scattering at two particles, or scatterers inside layered geometries, for which no analytic solutions are available. For such problems MMP is perfect for providing reference solutions. Note that its concept may be considered as a generalization of the Mie solution without a restriction concerning the shape and number of scatterers. For smooth geometries, MMP can provide solutions with arbitrarily high accuracy within reasonable time. Therefore, we use the MMP solver contained in OpenMaXwell [17] for getting reference solutions. More importantly, the contribution from the Ph.D work of A.Alparslan [21] makes

it possible to study smooth plasmonic particles inside layered geometries using an extension of MMP. His work has great value of providing highly accurate reference solutions in layered media, which would be very difficult to obtain using an analytical approach.

In summary, we focus on a FEM domain discretization solver and we use the help of a boundary solver for getting reference solutions.

2.2.3 Structured and unstructured meshes

In the area of domain discretization methods, there are two categories of meshes: structured and unstructured meshes, whereas all well-known boundary discretization methods work with unstructured meshes (*e. g.* BEM) or are mesh-free (MMP).

Structured meshes

In structured meshes, the computational domain is usually subdivided by rectangular grids. There are several advantages of the structured meshes. First of all, the implementation is very simple. The locations of grid points must not be stored because their indices indicate the positions. However, severe staircasing effects [34] make structured meshes inappropriate for plasmonics.

Take the most important solver, FDTD, as an example. The advantage of FDTD is that it directly discretizes the first order Maxwell equations by a coupled system of finite differences equations. By using central differences, second order accuracy is obtained with the same numerical effort as for first order finite difference schemes. FDTD is easy to implement, also for parallel computing. As mentioned above, the staircasing effect [34] is one of the biggest disadvantages. When the objects are curved, the rectangular grids will not represent the exact geometry and thus cause the staircasing effect at the material interfaces. Furthermore, when the fields change rapidly, very fine gridding is needed to resolve the space-time variation. The subgridding technique [35] can relieve this problem, but it makes the solver more complicated and leads to first order schemes. It also makes the time steps and the evaluations of the locations of the nodes more complicated.

Unstructured meshes

In un-structured meshes, the computational domain is subdivided into mesh elements, which are a set of patches that constitute an approximation of the whole computational domain. Unstructured meshes do not restrict the mesh. Therefore they can describe complicated objects much more precisely than structured mesh. Obviously, the storage of the mesh structure is much more demanding

than the storage of a structured mesh. Additional efforts are needed to obtain good meshes that do not cause numerical problems. Most of the existing commercial FEM softwares, *e. g.* COMSOL [36], have mature mesh generators to generate meshes of high quality. There are also many open source mesh generators, such as EZ4U [37]. Both EZ4U and the COMSOL mesh generator are used in this thesis.

The most prominent type of solvers using unstructured meshes is FEM [12], but FVTD and DG also use unstructured meshes.

For plasmonics

As mentioned above, structured meshes are not good for plasmonics, because their disadvantages are severe: In plasmonics, the objects are usually curved. Their approximation with structured meshes leads to the staircasing effect. Furthermore, strong field localizations are exploited in plasmonics, which implies that the fields change rapidly and this demands very fine discretization. Consequently, FEM with unstructured meshes is used in this thesis.

2.3 Selection of elements

Straight and curvilinear elements

In plasmonics, it is a great advantage to use curvilinear elements, since the objects are usually curved. Curvilinear elements provide accurate, or even exact, representations of the curved boundaries of the plasmonic objects. The two major advantages are as follows. Firstly, with curvilinear elements, one can save much effort to discretize curved boundaries. For straight elements, a very fine mesh is needed when the boundaries are curved. Curvilinear elements have edges which approximate the boundaries much better. Therefore less effort of refinement is needed. Secondly, curvilinear elements provide better accuracy. When performing the boundary integration on the edges of the curvilinear elements, the integration paths are posed on the curves which approximate the real boundaries or even on the exact boundaries. Straight edges provide worse approximations of the boundaries of the objects. Therefore, more errors are introduced in the boundary integrals when using straight elements. This comparison is illustrated in figure 2.2. In figure 2.2c, the integration is performed on the real boundary and therefore it is more accurate. In figure 2.2a, the integration is performed on the approximated straight edge that is away from the real boundary, thus it will introduce errors. It should be noted that the commercial software COMSOL can support geometry shape order up to quintic (5th-order) in the graphical user interface, while in this thesis, we study elements with circular curved edges.

FEM solvers use different kinds of elements. The following comparisons are of interest in this thesis.

Low and high orders elements

Most FEM solvers use polynomial basis functions. The order of the basis functions is an important issue.

For curvilinear elements, it is favorable to use higher orders. The order of the element should be matched by the order of boundary approximation. This issue is illustrated in figure 2.2. If one uses high order basis functions but straight elements, the quadrature points will not be placed on the real boundary, and therefore it is not beneficial (figure 2.2b). While figure 2.2c shows that the quadrature points of curvilinear elements are posed exactly on the real boundary.

Another important issue concerns the field singularities. In plasmonics, sharp corners theoretically cause field singularities. Near them small elements with low orders are beneficial. In practice, sharp corners do not exist and the field singularities are lifted by appropriate rounding. A class of more complicated problems is the triple points problem, where three different materials intersect. Many severe numerical problems appear. A good strategy is to both increase the polynomial degrees and refine the mesh.

There are many important issues of the combination of increasing the polynomial degrees (p -refinement) and decreasing the mesh size (h -refinement). This combination is called hp -FEM [38]. In general, big elements with high order

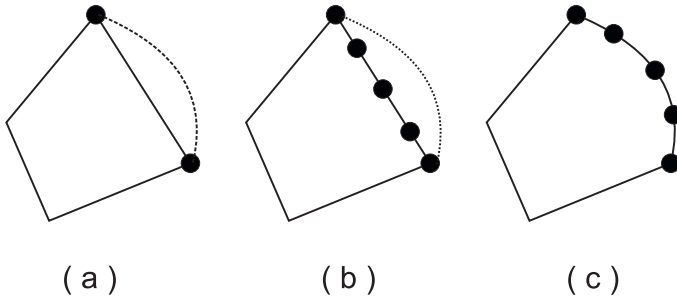


Figure 2.2: Comparison of straight and curved elements. The dots are quadrature points on one edge. The curved lines in a) and b) represent the real boundaries of the objects. a) straight element of order 1. b) straight element of order 4. c) curved element of order 4.

basis are good for modeling smooth fields, while small elements with low order basis are good for modeling singularities such as triple points and corners. The related issue will be addressed in chapter 4.

It should be noted that the commercial software **COMSOL** can support polynomial order up to cubic (3rd-order) in the graphical user interface, while in this thesis, we use a polynomial basis of arbitrary order.

Triangular and quadrilateral elements

In existing solvers, 2D elements usually are triangles or quadrilaterals. The triangular elements are mapped from a reference triangle, while the quadrilateral elements are mapped from a square. The mappings are illustrated in figure 2.3. In plasmonics, it seems to be slightly advantageous to use quadrilateral elements because of the skin effect: It may be good to apply thin but long elements, therefore quadrilateral elements are beneficial. The details will be addressed in chapter 3.2. Moreover, the shape of the perfectly matched layers (PML) are often rectangular blocks, therefore it is more convenient to use quadrilateral elements. The details will be addressed in chapter 3.3.

There are many commercial or open source mesh generators. For example, the commercial software **COMSOL** has built-in mesh generators for both triangular and quadrilateral elements. The open source software **EZ4U** generates quadrilateral elements with good quality. In this thesis, we apply quadrilateral elements, which are obtained by the following means. Firstly, we use semi-automatic Python scripts. Secondly, we use the open source mesh generator **EZ4U**. Thirdly, we use **COMSOL** to generate meshes, and convert them to our format. Note that a **COMSOL** mesh is parametrically controllable. **COMSOL** assisted mesh generation

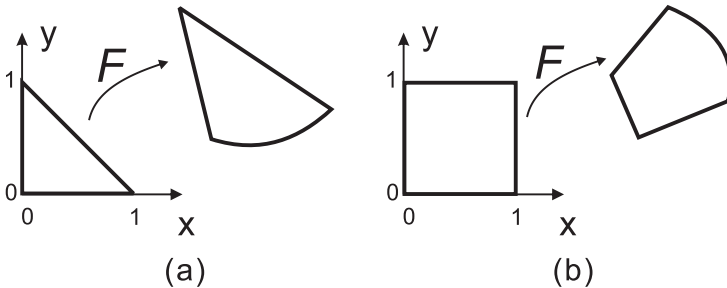


Figure 2.3: Mapping from the reference elements. F represents the mapping. a) mapping from the reference triangle. b) mapping from the reference square.

is developed in chapter 4

2.4 CONCEPTs

From the discussions above, we choose the FEM solver **CONCEPTs** as a promising candidate [13, 14, 15, 16]. **CONCEPTs** is an open source C++ library, which uses high polynomial basis functions and curved quadrilateral elements. More importantly, it supports hp-FEM [38].

The p -FEM strategy means that higher accuracy is obtained by increasing the orders of the basis functions. The basis functions of each order are constructed as products of 1D basis functions based on Jacobi polynomials in both directions of the reference square $[0, 1]^2$, which are then mapped to the physical element in the mesh [14, Chapter 9] [39]. Then, the matrix entries are computed by numerical quadrature on the reference square.

With limited order of the basis functions, higher accuracy can also be obtained by making the mesh finer while keeping the order of the basis functions fixed. This strategy is called h -FEM [38]. Simple non-curved elements are often used, where the curved interfaces need to be resolved by a finer discretization in order to obtain similar accuracy.

Using h -FEM with linear or quadratic basis functions leads to a low algebraic convergence in the number of degrees of freedom. This is in contrast with a p -FEM strategy with curved elements, which gives exponential convergence for piecewise smooth solutions [15, 40].

3 Truncation techniques

3.1 Introduction

In this chapter, we study the truncation techniques for FEM simulations of plasmonics. When solving Maxwell's equations in an infinite domain using finite elements, the domain must be truncated. The bounded interior region is separated from the unbounded exterior domain by an artificial boundary on which appropriate boundary conditions must be imposed to incorporate the effect of the exterior domain. The currently most popular approaches based on differential (local) operators are perfectly matched layers (PML) and absorbing boundary conditions (ABC). PML can easily be extended to complicated cases, but the effect of ABC/PML parameters on the solution accuracy is better understood for ABC.

We derive the variational formulation of ABC and PML, and implement them in the high-order FEM library `CONCEPTS`. We study scattering problems in free space and in presence of substrates and multilayer structures that support guided waves. The performances of ABC and PML are studied and a convergence analysis is performed.

3.2 Absorbing Boundary Conditions (ABC)

Absorbing boundary conditions have previously been used in low- and high-order finite element schemes [41, 42]. However, the rapid variation of the field at a plasmon resonance increases the computational effort necessary for obtaining a desired accuracy. Simulations of optical structures close to a plasmon resonance therefore require the development of a very efficient finite element solver.

Finite element methods are based on piecewise polynomial approximations of the solution of a partial differential equation. We can improve the quality of an approximation by a so-called h -FEM strategy, *i. e.*, decreasing the mesh size h for fixed polynomial degree p . Alternatively, a p -FEM strategy can be used, *i. e.*, fix the mesh size h and increase the polynomial degree p . It is well known that p -FEM is superior when the field is smooth, but a local mesh refinement is necessary in areas with very rapid variation of the field. This combination of h -refinements and p -refinements is called hp -FEM [40, 43].¹

¹This part was essentially published in [7]

3.2.1 Scattering problem and BGT conditions

A two-dimensional scattering problem is studied where the electromagnetic waves propagate in a non-magnetic material, $\mu = \mu_0$, with the relative permittivity $\epsilon(x, y) = \epsilon(\vec{x})$ independent of the third coordinate z .

As usual, the electromagnetic wave (E, H) is decomposed into transverse electric (TE) waves $(E_1, E_2, 0, 0, 0, H_3)$ and transverse magnetic (TM) waves $(0, 0, E_3, H_1, H_2, 0)$ [27]. This decomposition reduces the full 3D Maxwell equations to scalar 2D Helmholtz equations in H_3 and in E_3 .

In the optical regime, a surface plasmon resonance can be excited if a noble metal is illuminated by a transverse electric (TE) wave [10]. We consider TE-waves with magnetic polarization $H(\vec{x}) = (0, 0, u)$, where u denotes the total field, and denote the wave number of the impinging wave by k_0 . The following equations characterize the scattering problem for the TE polarization,

$$\begin{aligned} -\nabla \cdot \left(\frac{1}{\epsilon(\vec{x})} \nabla u(\vec{x}) \right) - k_0^2 u(\vec{x}) &= 0, \quad \vec{x} \in \Omega \\ u &= u^{sc} + u^{inc}, \\ \lim_{r \rightarrow \infty} r^{1/2} \left(\frac{\partial u^{sc}}{\partial r} - ik_0 u^{sc} \right) &= 0, \end{aligned} \quad (3.1)$$

where u^{sc} and u^{inc} denote the scattered field H_3^{sc} and the incoming field H_3^{inc} , respectively.

Due to the discontinuity of the piecewise constant permittivity $\epsilon(\vec{x})$, the field will change rapidly across the material interface.

The last condition in (3.1) is the Sommerfield radiation condition [44], which characterizes outgoing waves. However, this condition is in the far field limit $r \rightarrow \infty$ and can not be numerically implemented. Absorbing boundary conditions are therefore applied on the boundary of a truncated domain Ω of radius R ; see Figure 3.1. The Bayliss-Gunzburger-Turkel (BGT) conditions are derived based on an asymptotic expansion in $k_0 R$ and are therefore accurate when $k_0 R$ is large enough [45]. The 0th to 2nd BGT conditions in polar coordinates are

$$\frac{\partial u^{sc}}{\partial r} + \alpha u^{sc} + \beta \frac{\partial^2 u^{sc}}{\partial \theta^2} = 0, \quad r, \theta \in \Gamma_0, \quad (3.2)$$

where the parameters α and β are given in Table 3.1.

Note that another approach is the Dirichlet-to-Neumann (DtN) mapping, which is even more accurate.

3.2.2 Finite elements formulation and discretization

The computational domain Ω (Figure 3.1), consists of the region of the scatterer Ω_ϵ surrounded by air Ω_0 . The BGT condition is applied on the circle Γ_0 of radius

Type	α	β
BGT-0	$-ik_0$	0
BGT-1	$-ik_0 + \frac{1}{2R}$	0
BGT-2	$-ik_0 + \frac{1}{2R} - \frac{1}{8R(1-ik_0R)}$	$-\frac{1}{2R(1-ik_0R)}$

Table 3.1: The coefficients of the BGT absorbing boundary conditions in (3.2).

R .

Following the standard procedure for the Galerkin method, the first equation in (3.1) is multiplied with a test function v and integrated over Ω . After integration by parts we obtain

$$\int_{\Omega} \frac{1}{\epsilon(\vec{x})} \nabla u \cdot \nabla v \, d\vec{x} - k_0^2 \int_{\Omega} uv \, d\vec{x} - \int_{\Gamma_0} \partial_n uv \, ds = 0, \quad (3.3)$$

where we use the fact that Γ_0 is located outside the scatterer, which is a region of relative permittivity one, i.e. $\epsilon(\vec{x})|_{\vec{x} \in \Gamma_0} = 1$.

We apply a second order ABC (3.2) to the total field u . The condition on the circular artificial boundary then takes the form

$$\partial_n u = \left(-\alpha u - \beta \frac{\partial^2 u}{\partial \theta^2} \right) + \left(\alpha u^{inc} + \partial_n u^{inc} + \beta \frac{\partial^2 u^{inc}}{\partial \theta^2} \right). \quad (3.4)$$

From (3.3) and (3.4) it follows that the variational formulation of TE scattering problems with the BGT boundary condition is as follows: Find a function u

such that

$$a(u, v) = b(v), \quad (3.5)$$

holds for all test functions v , where the sesquilinear form $a(u, v)$ and the linear form $b(v)$ are

$$a(u, v) = \int_{\Omega} \left(\frac{1}{\epsilon(\vec{x})} \nabla u \cdot \nabla v - k_0^2 uv \right) d\vec{x} + \int_{\Gamma_0} \left(\alpha uv + \beta \frac{\partial^2 u}{\partial \theta^2} v \right) ds, \quad (3.6)$$

and

$$b(v) = \int_{\Gamma_0} \left(\alpha u^{inc} + \partial_n u^{inc} + \beta \frac{\partial^2 u^{inc}}{\partial \theta^2} \right) v ds. \quad (3.7)$$

We refer to [46] for a more detailed mathematical description of the variational problem (3.5). More detailed formulation is addressed in Appendix A.

The edge integral $\int_{\Gamma_0} \frac{\partial^2 u}{\partial \theta^2} v ds$ can not be implemented directly. However, due

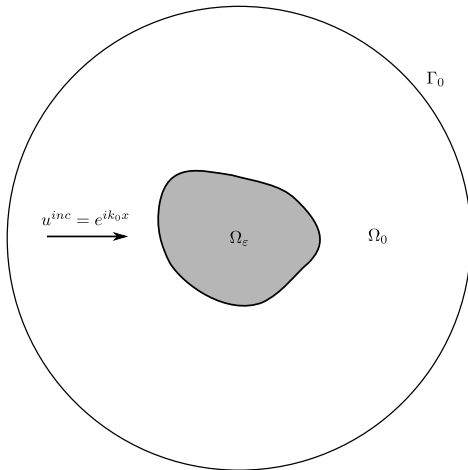


Figure 3.1: Computational domain Ω with the region of the scatter Ω_ϵ and artificial circular boundary Γ_0 .

to the fact that Γ_0 is closed, integration by parts gives

$$\int_{\Gamma_0} \frac{\partial^2 u}{\partial \theta^2} v \, ds = - \int_{\Gamma_0} \frac{\partial u}{\partial \theta} \frac{\partial v}{\partial \theta} \, ds + 0. \quad (3.8)$$

On the circular boundary Γ_0 , the tangential derivative is

$$\frac{\partial}{\partial \theta} = R \frac{\partial}{\partial s}.$$

Therefore the edge integral becomes

$$\int_{\Gamma_0} \frac{\partial^2 u}{\partial \theta^2} v \, ds = - \int_{\Gamma_0} R^2 \frac{\partial u}{\partial s} \frac{\partial v}{\partial s} \, ds.$$

If one chooses an absorbing boundary on a curve other than a circle, *e. g.*, an ellipse, the formulation and implementation will be more complicated [47, 48]. Despite of this, the elliptic absorbing boundary is more efficient than the circular one for long shape scatterers. In this paper, we only apply ABC on a circular absorbing boundary, which is sufficient for the problems under study.

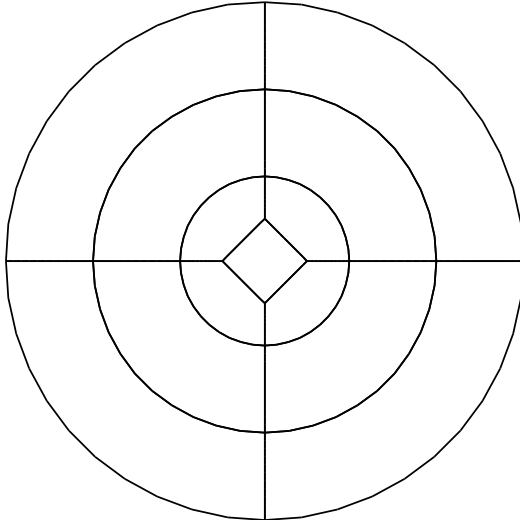


Figure 3.2: CONCEPTs mesh with 13 curved quadrilateral cells used in the p -FEM computations with CONCEPTs.

For the discretization of (3.5) we use the C++ library `CONCEPTs` [13, 15, 16] (www.concepts.math.ethz.ch). The `CONCEPTs` package uses high polynomial basis functions and curved quadrilateral elements. We use curved elements because its edges can resolve the circular material interface exactly. As a result, the quadrature points of the high polynomial basis follow the material interface by which the approximation order of the high order polynomial basis is retained. Figure 3.2 shows the `CONCEPTs` mesh, which contains 13 curved quadrilateral elements. We use the p -FEM strategy, which means the higher accuracy is obtained by increasing the orders of the basis functions [40]. The basis functions of each order are constructed as products of 1D basis functions based on Jacobi polynomials in both directions of the reference square $[0, 1]^2$, which are then mapped to the physical element in the mesh [14, Chapter 9] or [39]. Then, the matrix entries are computed by numerical quadrature on the reference square. Note that the used basis with moderate matrix conditioning [49]. Similar bases can be constructed for (vectorial) edge elements on quadrilaterals and hexahedra for full Maxwell systems [50].

In all computations we have used the direct solver SuperLU [51]. A direct solver can be used for larger systems with p -FEM than with h -FEM as the number of degrees of freedom remains moderate for high accuracy. For very

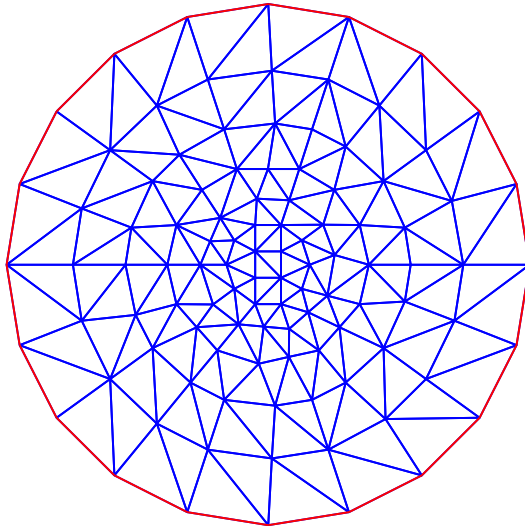


Figure 3.3: Example of triangular mesh generated by FreeFEM++.

large problems, especially in 3D, iterative solvers are potentially more efficient.

Many finite element packages and commercial softwares use linear or quadratic basis functions on triangular meshes such as in Figure 3.3, which is generated by FreeFEM++

(www.freefem.org/ff++). With this limited set of basis functions, higher accuracy is obtained by making the mesh finer while keeping the order of the basis functions fixed. This strategy is called h -FEM [40]. Often simple non-curved elements are used, where the curved interfaces need to be resolved by a discretization with more elements, in order to obtain similar accuracy.

Using h -FEM with linear or quadratic basis functions leads to a low algebraic convergence in the number of degrees of freedom. This is in contrast with a p -FEM strategy with curved elements, which gives exponential convergence for piecewise smooth solutions [15, 40], in the number of degrees of freedom, in the number of nonzero entries in the system matrix as well as in the computation time. The system matrices for p -FEM are less sparse than for h -FEM. If the mesh includes mainly non-parallellogram cells, the ratio of the number of non-zero and the total number of matrix entries depends only on the number of cells.

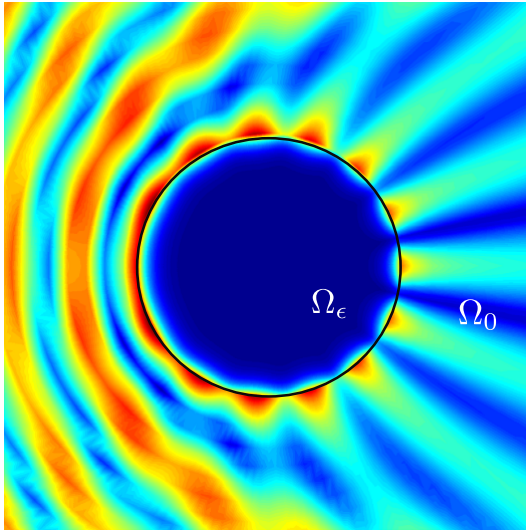


Figure 3.4: The absolute value of total magnetic field, with 2596 degree of freedom. The radius of the silver wire is 400nm, and the wavelength is 413nm. The permittivity of silver $-5.0092942+0.2194588i$, is calculated from the Drude model (3.9). A strong surface plasmon resonance is observed.

It does not decrease when p increases. The reason is that for non-parallelogram cells, for example, generally curved cells, the orthogonality relation derived on the reference element does not transform to the physical cell. Nevertheless, to achieve the same accuracy the number of degrees of freedom for h -FEM increases much faster than for p -FEM, leading to the fact that p -FEM works with smaller, but more densely populated matrices.

3.2.3 Numerical results and discussions

Scattering from one cylinder

We compute the scattering from a silver circular wire illuminated by an incoming plane wave at an optical frequency. The problem was previously studied in [52], where the performance of low-order finite elements was compared with several integral equation based solvers. In the numerical experiments, we implement the second order BGT boundary condition in `CONCEPTs` and use high order curvilinear elements.

The geometry and the material model are taken from [52], *i. e.*, silver is characterized as a homogeneous material described by the Drude Model [27, 28]:

$$\epsilon(\omega) = \epsilon_\infty - \frac{\omega_p^2}{\omega(\omega + i\Gamma)}, \quad (3.9)$$

$$\epsilon_\infty = 5, \quad \omega_p = 1.4433 \times 10^{16} \text{ rad/s}, \quad \Gamma = 10^{14} \text{ rad/s}.$$

At wavelength 413nm, (3.9) gives that the permittivity of silver is $-5.00929 + 0.21946i$.

We first compute the scattering from one cylinder of radius 400nm, with the mesh of 13 curvilinear elements shown in Figure 3.2. The second order BGT boundary condition is set on Γ_0 , which is located two wavelengths away from the scatterer. The polynomial degree of the basis is 15, resulting in 2596 degrees of freedom. The absolute value of the total magnetic field is shown in Figure 3.4, where one can observe a strong surface plasmon resonance on the surface of the scatterer.

The strong resonance is due to the large negative real part and small positive imaginary part, which result in a strong surface plasmon resonance [52].

To validate the FEM results, we compare the field values along the surface of the cylinder with those obtained from MMP, which coincides with the analytical Mie solution and provides a solution with machine precision when the number of multipole and Bessel orders is high enough. The required order depends on the radius of the cylinder, its material properties, and on the wavelength. Because of the exponential convergence and internal error checking capabilities of MMP, one easily may find the required multipole order. Since the cylinder considered in the test case is rather large, quite high orders are required. For maximum

multipole order 27, the MMP solution has 56 degrees of freedom and reaches in average a relative error below $1.2 \times 10^{-13}\%$, *i. e.*, machine precision is reached. For maximum order >27 almost the same error is obtained, *i. e.*, the error does not decrease further for higher multipole orders. Note that the highest errors are usually obtained in the close vicinity of the interface between two different materials. Therefore, the comparison of the field values on the surface of the cylinder is a much harder test than, for example, a comparison of the far field. It should be also mentioned that the relative error is usually the highest at points where the field is rather weak. Thus, the maximum relative errors may be considerably higher than the average relative errors. In the considered test case, the maximum relative error is below $4 \times 10^{-13}\%$, *i. e.*, also very low, which provides high confidence in the reference results.

The comparison between **CONCEPTs** and MMP is shown in Figure 3.5. A very good agreement is achieved with only 2956 degrees of freedom and therefore very little computational effort. Notice that the degrees of freedom in MMP and finite elements can not directly be compared since discretization with MMP results in full matrices whereas the FE discretization results in sparse matrices. Compared with low order non-curved finite elements, high order basis functions with curved elements are more efficient for problems with curved material interfaces.

With the mesh fixed, we increase the order of basis function to study the p -FEM convergence. The relative L^2 error is computed within the region Ω_E

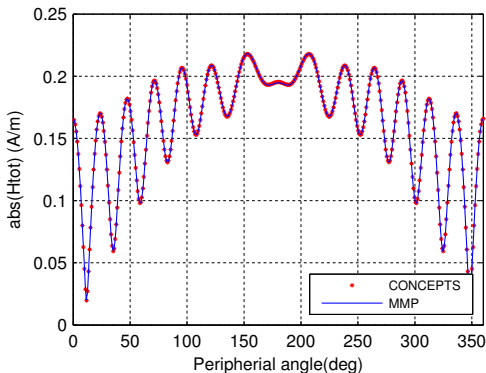


Figure 3.5: The comparison of $|H^{\text{total}}|$ across the material interface, between **CONCEPTs** results and MMP results. The mesh is shown in figure 3.2 with the degrees of freedom 2956, and the absorbing boundary is 2λ away from the scatterer.

of radius $R_0 + 2/3\lambda$. That is, we compute the ratio between the L^2 norm of $u - u_{ref}$ and u_{ref} :

$$\text{relative } L^2 \text{ error} = \frac{\sqrt{\int_{\Omega_E} |u - u_{ref}|^2 d\vec{x}}}{\sqrt{\int_{\Omega_E} |u_{ref}|^2 d\vec{x}}},$$

where u_{ref} denotes the MMP reference solution. The reasons of taking relative L^2 -error only in the near field region Ω_E are twofold: Firstly, one can compute the far-field information from the near-field pattern, secondly, for the plasmonic devices, the near field behavior is of high interest.

We study the problem with different radii of the absorbing boundary. For each radius, the p -convergence is studied. We increase the polynomial degree of the basis from 1 to 29 with an increment of 2. For each step, the relative L^2 error is computed, and the degrees of freedom and the consumed time are recorded. We perform these simulations using one core of a $4 \times 2.4\text{GHz}$ Intel quad-core machine, with 8GB RAM. The final test of polynomial degree 29 uses 10992 degrees of freedom, and takes 326 seconds. The convergence results are shown in Figure 3.6, where one can observe the following properties:

For low degrees of freedom the relative error remains practically at 100 %. In this range the wave is resolved with less than 3 degrees of freedom per wavelength and utterly wrong. This phase with low accuracy is longer if the computational domain is larger. However, when a certain minimum resolution is reached

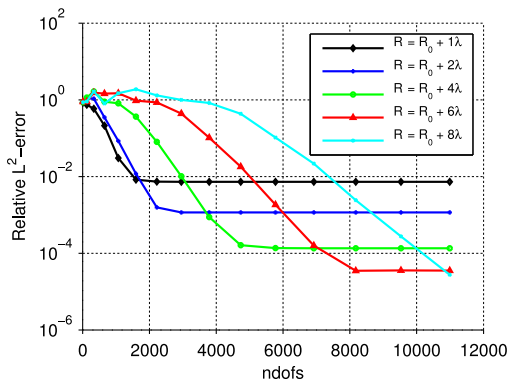


Figure 3.6: p -FEM convergence. The distance between the boundary and the scatterer is 1,2,4,6, and 8 times of the wavelength, respectively.

a fast convergence follows [53], with more rapid convergence for a smaller computational domain. Finally, the convergence stops at a limited accuracy, which is determined by the radius of the absorbing boundary and can be explained as the model limitation of the asymptotic expansion in the BGT condition. This is a drawback compared with PML, where the absorbing layers can be placed very close to the scatterer, however, for the price of more degrees of freedom to model the PML layer. Recent research shows that high-order ABC may have favorable complexity estimates relative to PML [54].

We observe that a higher accuracy can be reached if the absorbing boundary is put further away from the scatterer. This is a consequence of the asymptotic nature of the BGT conditions [45], for which the error decays with the radius and for increasing wave numbers. However, there is a trade-off between the higher model accuracy and the higher computational complexity of a larger computational domain. If the absorbing boundary is further away, the convergence will be slower, since more degrees of freedom are consumed to resolve the solution in free space. This tells us that the accuracy of a numerical solution can be improved by enlarging the computational domain, and as a result, the computational costs will increase as well.

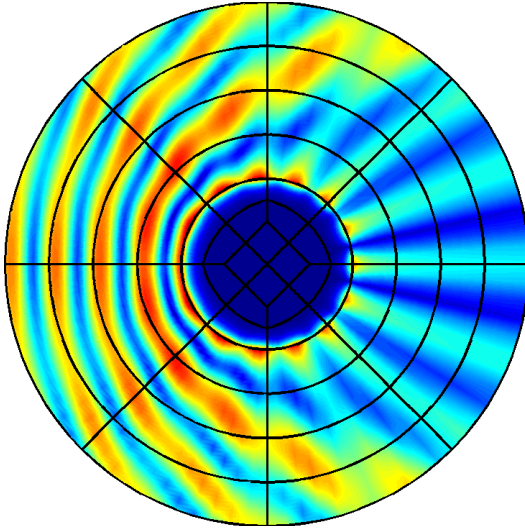


Figure 3.7: A finer mesh and the solution. This mesh, consisting of 52 elements, is obtained after one step of uniform h -refinement based on the mesh in Figure 3.2.

This observation also suggests that we would benefit from using an adaptive strategy. One can follow the fast convergence of a small computational domain at the beginning, then after the convergence stops, increase the domain size for a further convergence to reach a better accuracy. This algorithm behaves like a tracing strategy, that finds the bottom in the convergence plot in Figure 3.6.

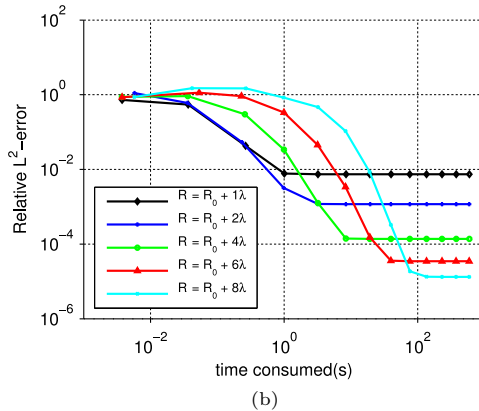
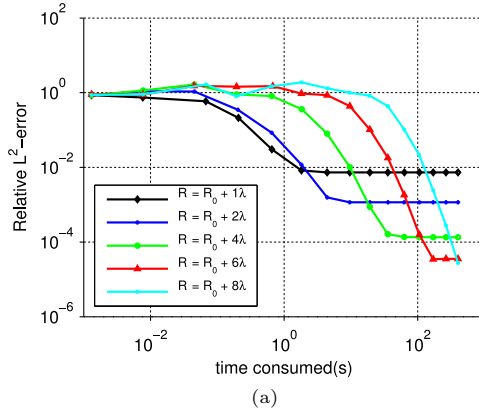


Figure 3.8: The relationship between computation time and relative L^2 error from scattering of one cylinder: (a) with the mesh shown in Figure 3.2, and (b) with the finer mesh in Figure 3.7.

However, this is not easy for arbitrary problems, where the solution is unknown. Then one must find a way to know when the convergence slows down.

In order to find the factors that influence the efficiency of the numerical method and using ABC, we compute the relative L^2 errors with respect to the time consumption. We first use the mesh in Figure 3.2 and then a finer mesh in Figure 3.7, which is obtained after one step of uniform h -refinement of the mesh in Figure 3.2, and has therefore four times more elements. The convergence plots with respect to the time indicating the efficiency are shown in Figure 3.8.

We observe that the errors decay faster for the finer mesh when increasing the polynomial degree. In fact with the finer mesh the same error is obtained with smaller polynomial degrees, and that for lower computational cost. For example the green curves in Figure 3.8 stop at the same error level indicating the modeling error of the ABC with outer radius $R_0 + 4\lambda$. For the coarse mesh this saturation level is reached with $p = 19$ (and 4732 degrees of freedom) and with a computation time $t = 36$ s, whereas it is reached for the finer mesh already with $p = 11$ (and 6337 degrees of freedom), but within $t = 8.4$ s only. The reason of the higher computational effort per degree of freedom is the lower sparsity of the system matrices when using high polynomial degrees on a coarser mesh. More basis functions overlap than with lower polynomial degrees on a finer mesh. This lower sparsity would be less emphasized when we would have used non-curved trapezoidal or even parallelogram shaped elements due to orthogonality of a larger number of basis functions. The lower computational effort for finer meshes and lower polynomial degrees is punished with a lower asymptotic convergence rate, which is not visible in our example as the accuracy is limited by the ABC.

Scattering from two cylinders

The scattering of two cylinders is a more demanding problem than that of one cylinder, namely when the gap is very narrow with respect to the radius of the cylinders, which makes the meshing difficult and causes a strong plasmonic interaction with a very high field enhancement in the gap area. The latter is attractive for practical applications. This strong interaction has also an impact on the analytic Mie solution. Theoretically, one may model the scattered field with two multipole expansions, located in the centers of the two cylinders. Furthermore, one may model the field inside each cylinder by a Bessel expansion as for the single cylinder case. This extended Mie solution should also converge exponentially because the boundaries of the cylinders are still circular. However, exponential convergence does not mean that the multipole order required to obtain machine precision is low or even similar to the order required for the single cylinder case. It turns out that severe numerical problems occur due to cancellation effects and in the computation of high multipole and Bessel orders.

Therefore, one cannot even reach a reasonable accuracy of a few digits when double precision numerics is used. MMP now offers the opportunity to account for the strong interaction by placing additional multipoles located near the gap area. Furthermore, one may take the symmetry into account. Then one must model only one of the two cylinders explicitly. With two or more "auxiliary" multipoles located near the gap, in addition to a multipole and Bessel expansion located in the center of the cylinder. One then reaches machine precision with multipole order 45, *i. e.*, 364 degrees of freedom, for the considered configuration.

In the finite element computation, we implement a second order BGT condition, which is put eight wavelengths away from the scatterer. The mesh is shown in Figure 3.9, and the absolute value of the total magnetic field is shown in Figure 3.10, where one can observe strong local field enhancement in the gap area. There is no analytical solution for this problem. Therefore MMP is a valuable source for generating reliable reference solutions. In Figure 3.11, the comparison of $|\mathbf{H}^{\text{total}}|$ across the material interface of the upper cylinder is shown, where a very good agreement is achieved. However, unlike the one cylinder scattering, the computation is not cheap. We compute on an i7-980X Intel machine with 24GB RAM, using 13409 degrees of freedom. Using one core,

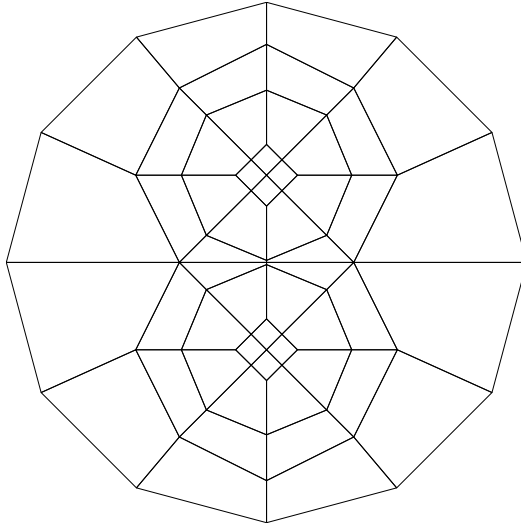


Figure 3.9: The CONCEPTs mesh of the two cylinders computation example. The mesh consists of 52 cells.

the computation time is 17.4 seconds to achieve the accuracy in Figure 3.11.

As for the one cylinder problem, the convergence behavior is studied for the two cylinders case. The relative L^2 error is computed on Γ , which is the material interface of the upper cylinder. That is, we compute the ratio between the L^2 norm of $u - u_{ref}$ and u_{ref} :

$$\text{relative } L^2 \text{ error} = \frac{\sqrt{\int_{\Gamma} |u - u_{ref}|^2 d\vec{x}}}{\sqrt{\int_{\Gamma} |u_{ref}|^2 d\vec{x}}},$$

where u_{ref} denotes the MMP reference solution. The convergence results are shown in Figure 3.12.

Firstly, we study the p -convergence for different sizes of the absorbing boundary, and the results are shown as solid lines in the figure. We can observe similar properties as in the scattering problem for one cylinder.

Secondly, in order to compare p -FEM with h -FEM, we perform an h -convergence analysis. The absorbing boundary is put 4λ away from the scatterer and we use

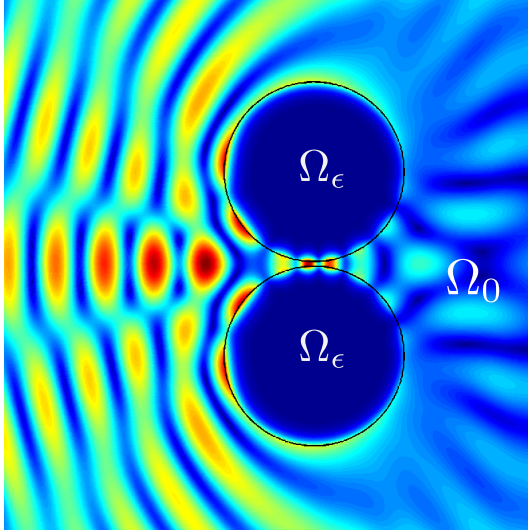


Figure 3.10: The absolute value of total magnetic field. The radius of the silver wire is 400nm and the gap between the two wires is 20nm, with incoming wave of wavelength 413nm. A strong local enhancement can be observed in the gap area.

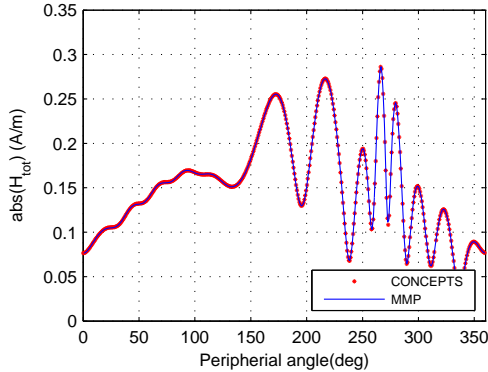


Figure 3.11: Comparison between MMP and CONCEPTs results of $|H^{\text{total}}|$ in the two cylinder case, the values are taken across the the material interface of the upper cylinder. The absorbing boundary is 4λ away from the scatterer, and the computation consumes 13409 degrees of freedom.

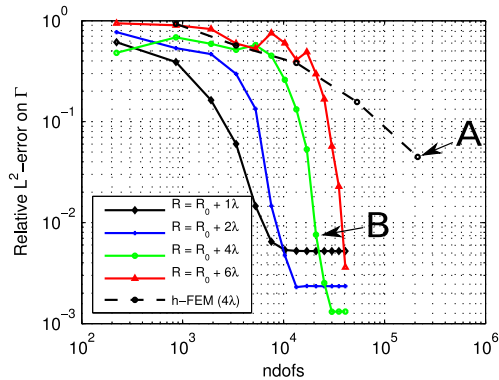


Figure 3.12: Convergence for the two cylinders case. The solid lines represent the p -convergence for the boundary $1, 2, 4$, and 6λ away from the scatterer, respectively. The dashed line represents the h -convergence for the boundary 4λ away from the scatterer, using quadratic curvilinear finite elements. A and B are two selected computation examples in Figure 3.13.

quadratic curvilinear finite elements, which is commonly used in commercial and scientific softwares. The result is shown as the dashed line in the figure and it is obvious that p -FEM converges faster than h -FEM and consumes less degrees of freedom for this problem. Moreover, CONCEPTs was recently compared with FreeFEM++, which uses non-curved triangular elements [55]. This comparison shows the importance of using curved elements.

Sparsity and condition number

It is important to study the sparsity and the condition number for matrices resulting from discretizations with high order curvilinear finite elements [46]. We choose two computation examples of similar accuracies in Figure 3.12: Test case A is obtained by 5 steps of h -refinement with 213377 degrees of freedom, and reaches the accuracy 0.012, while test case B is obtained by 10 steps of p -refinement with 20921 degrees of freedom, and reaches the accuracy 0.0076. The system matrix structures are shown in Figure 3.13, from which we can observe that the matrices in both cases are sparse. The density, *i. e.*, the ratio between the number of nonzero matrix entries and the total number of matrix entries, of the matrices is 9.3×10^{-5} for case A, and 6.8×10^{-3} for case B. The condition numbers are 9.25×10^5 for case A, and 9.75×10^5 for case B, which are both very low. The high sparsity and low condition number imply that high order curvilinear finite element will also have good performance in large 2D and 3D problems.

The situation for MMP is different. Like all boundary discretization methods, MMP leads to relatively small but full matrices that tend to be ill-conditioned. MMP works with an overdetermined system of equations and special procedures that can provide highly accurate results even when the condition numbers of the MMP matrices are higher than 10^{16} . The efficiency of MMP and similar boundary discretization methods is higher for low dimensions and increases with the smoothness of the interfaces. Therefore, MMP is highly attractive for 2D problems with not too complex geometry and for 3D problems with sufficiently smooth geometry. Thus, MMP is excellent for delivering reference solutions for scattering from objects with smooth interfaces. However, for 2D problems with complicated geometry and most of the 3D problems, FEM is more efficient than MMP.

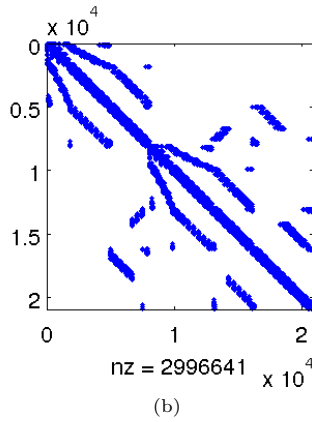
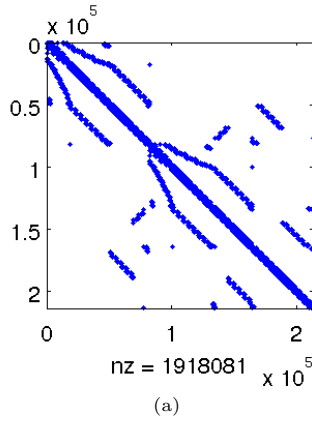


Figure 3.13: The structure of the system matrices: (a) for test example A in Figure 3.12, (b) for test example B in Figure 3.12.

3.3 Perfectly Matched Layers (PML)

Many plasmonic applications, such as nano antennas [1, 2], photonic crystals [3], and chemical and biological sensors [4, 5, 6], are usually mounted on or embedded in layered media. Their behavior may be strongly affected by the underlying substrate or multilayer structures.

In such structures we find guided and leaky waves [56], which are not present in the homogeneous exterior of scattering objects. The Sommerfeld radiation condition [57, 58] decides in homogeneous exterior, if a wave is outgoing or incoming, and guarantees in this way for a unique definition of purely outgoing scattered fields. Several conditions have been proposed to replace or extend the Sommerfeld radiation condition to multilayer structures, see *e. g.* [59, 60, 61, 62, 63, 64].

For the numerical analysis of scattering problem in unbounded multilayer structures the most important issue is the truncation of the domain. The direct application to layered structures has to face the problem of infinite interfaces. With the development of integration techniques for the evaluation of multilayer Green's functions [64, 65], formulations only on the boundary of the scatterer are possible, and such formulations have been successfully used with MMP [19]. For a homogeneous exterior there are various local absorbing boundary conditions [57, 58], which can be used with volume discretization methods like FEM or the finite difference time domain method (FDTD). Perfectly matched layers (PML), which is the most popular truncation technique, was first proposed in [66], and later introduced to FEM [67]. The introduction of PML can be considered as a complex coordinate stretching [68], which leads to exponentially decaying solutions. In FDTD, the geometry of the PML is naturally rectangular due to the structured mesh of FDTD. In 2D FEM, the typical shapes of PML blocks are rectangles and circular shells, which correspond to Cartesian [69] and radial PML [70], respectively. Motivated by the pole condition, PML have also been proposed for more general layered media [71]. To reduce the error, the thickness and mesh widths in the PML can be *a-posteriori* adapted [72, 73, 74, 75]. The Hardy space infinite elements [76] and the pole condition method [77, 78] are alternative methods for multilayer structures.

In this section, the modeling of multilayer scattering in the presence of guided modes is studied using FEM with an *hp*-adaptive PML discretization. The possibility to refine the mesh (*h*-refinement), to increase the polynomial order (*p*-refinement) or both (*hp*-refinement) even only in certain parts of the mesh (adaptive refinement) provides well-adapted refinement strategies [40]. Using those strategies, an error level can be reached with much lower number of degrees of freedom (DOFs) than with uniform mesh refinement and constant polynomial

degree.²

3.3.1 Finite element formulation and implementation

Finite element variational formulation using PML

We focus on two-dimensional scattering problems, where the electromagnetic waves propagate in a non-magnetic material, with the relative permittivity $\epsilon(x, y) = \epsilon(\vec{x})$. Here \vec{x} denotes the 2D coordinates (x, y) since the problem does not depend on the third coordinate z .

As usual, the electromagnetic wave (E, H) is decomposed into transverse electric (TE) waves $(E_x, E_y, 0, 0, 0, H_z)$ and transverse magnetic (TM) polarized waves $(0, 0, E_z, H_x, H_y, 0)$ [56, 27]. This decomposition leads to scalar 2D Helmholtz equations in H_z and in E_z . In the optical regime, a surface plasmon resonance can be excited if a noble metal is illuminated by a TE wave [10]. We therefore consider TE waves with magnetic polarization $\vec{H}(\vec{x}) = (0, 0, u^{\text{tot}})$, where u^{tot} denotes the total magnetic field, and we denote the wave number of the impinging wave $\vec{H}^{\text{imp}}(\vec{x}) = (0, 0, u^{\text{imp}})$ from above by k_0 .

For reasons of simplicity, we consider a plasmonic object within a multilayer structure as test case, which is illustrated in Figure 3.14. The multilayer structure is defined in \mathbb{R}^2 through its piecewise constant relative permittivity $\epsilon_{\text{mul}}(\vec{x})$ only varying in y direction. The permittivity ϵ_{mul} takes the values ϵ_{lay} in the substrate, ϵ_{coat} in coatings of the substrate to the top and bottom and 1.0 in the air region above and below the coatings. The scatterer Ω_{sc} with relative permittivity ϵ_{sc} and boundary Γ lies inside the substrate, and the overall permittivity $\epsilon(\vec{x})$ coincides with $\epsilon_{\text{mul}}(\vec{x})$ outside the scatterer and with ϵ_{sc} inside the scatterer.

We are going to use a scattered field formulation, in which the scattered field u^{sc} in the decomposition $u^{\text{tot}} = u^{\text{sc}} + u^{\text{inc}}$ is the unknown. For this we have to define a generalized incoming field $\vec{H}^{\text{inc}} = (0, 0, u^{\text{inc}})$ which solves

$$-\nabla \cdot \left(\frac{1}{\epsilon_{\text{mul}}(\vec{x})} \nabla u^{\text{inc}} \right) - k_0^2 u^{\text{inc}} = 0 \quad (3.10)$$

in the whole space \mathbb{R}^2 . Its incoming part from above is the impinging wave \vec{H}^{imp} and it is purely outgoing to the bottom. This generalized incoming field u^{inc} consists of the reflected and transmitted waves in each layer, and can be computed analytically [56].

²This part was essentially published in [8]

The scattered field u^{sc} solves

$$-\nabla \cdot \left(\frac{1}{\epsilon_{\text{mul}}(\vec{x})} \nabla u^{\text{sc}} \right) - k_0^2 u^{\text{sc}} = 0 \quad \text{in } \mathbb{R}^2 \setminus \Omega_{\text{sc}} \quad (3.11a)$$

$$-\nabla \cdot \left(\frac{1}{\epsilon_{\text{sc}}} \nabla u^{\text{sc}} \right) - k_0^2 u^{\text{sc}} = \left(1 - \frac{\epsilon_{\text{lay}}}{\epsilon_{\text{sc}}} \right) k_0^2 u^{\text{inc}} \quad \text{in } \Omega_{\text{sc}} \quad (3.11b)$$

$$[u^{\text{sc}}]_{\Gamma} = 0 \quad (3.11c)$$

$$\left[\frac{1}{\epsilon(\vec{x})} \nabla u^{\text{sc}} \cdot \mathbf{n} \right]_{\Gamma} = (\epsilon_{\text{sc}}^{-1} - \epsilon_{\text{lay}}^{-1}) \partial_n u^{\text{inc}}, \quad (3.11d)$$

and is purely outgoing to all sides. Here, $[\cdot]_{\Gamma}$ stands for the jump between field values outside and inside the scatterer. As the multilayers approach infinity and the scattered field may incorporate outgoing guided modes to the left and right, which do not decay, the Sommerfeld radiation condition [57, Chap. 1], [58, Chap. 3] does not apply. Instead the outgoing nature of u can be enforced by more general radiation conditions [59, 60, 61, 62], the pole condition [63] or by means of the multilayer Greens functions [64, 65]. For applying the pole condition and the PML, one has to exclude guided waves with different directions of group and phase velocities, which do not exist in non-dispersive dielectric multilayer structures.

We are interested to obtain the scattered field in a rectangular region of interest Ω around the scatterer Ω_{sc} (see Figure 3.14).

Following the standard procedure for the Galerkin method, equation (3.11a) is multiplied with a test function v and integrated over Ω . After integration by parts, we obtain the equation

$$\begin{aligned} & \int_{\Omega} \frac{1}{\epsilon(\vec{x})} \nabla u^{\text{sc}} \cdot \nabla v \, d\vec{x} - k_0^2 \int_{\Omega} u^{\text{sc}} v \, d\vec{x} - \int_{\partial\Omega} \frac{1}{\epsilon(\vec{x})} \partial_n u^{\text{sc}} v \, ds \\ & = k_0^2 \int_{\Omega_{\text{sc}}} \left(1 - \frac{\epsilon_{\text{lay}}}{\epsilon_{\text{sc}}} \right) u^{\text{inc}} v \, d\vec{x} + \int_{\Gamma} (\epsilon_{\text{lay}}^{-1} - \epsilon_{\text{sc}}^{-1}) \partial_n u^{\text{inc}} v \, ds. \end{aligned} \quad (3.12)$$

This equation is not complete, since no boundary conditions are specified. Therefore, we enlarge the computational domain by a PML layer. By applying the PML coordinate transformation, one can obtain the variational formulation in the whole computational domain $\Omega_0 := \Omega \cup \Omega_{\text{PML}}$, which is a box-shaped domain for the Cartesian PML. The details of the transformation can be found in [69].

The transformation leads to a transformed scattered field outside Ω , which is exponentially decaying away from the PML interface $\partial\Omega$ and is almost zero on $\partial\Omega_0$, if the PML layer is thick enough. Therefore, we neglect the corresponding boundary term on $\partial\Omega_0$ corresponding to homogeneous Neumann boundary

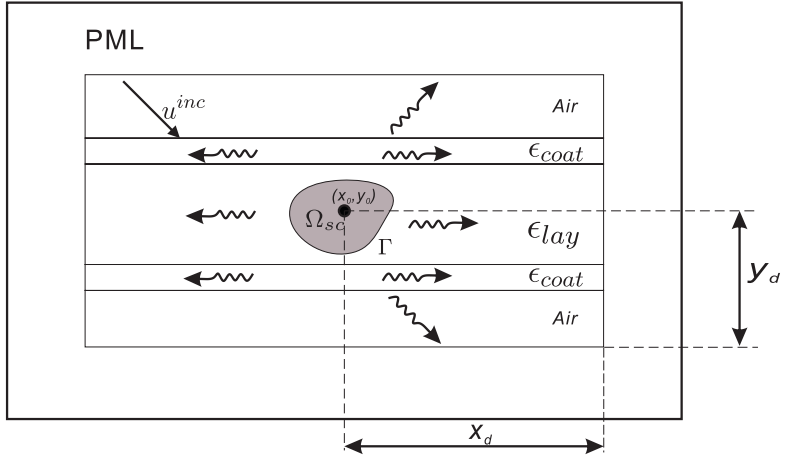


Figure 3.14: Scattering from the multi-layered test structure, illuminated by a plane wave from top. Scattered and guided waves can be excited. The physical domain is surrounded by a PML.

conditions. The unknown of the resulting variational formulation u shall be an approximation to u^{sc} in Ω and exponentially decaying in Ω_{PML} . Then, the problem reads:

$$\text{find } u \in H^1(\Omega_0), \text{ s. t. } \Phi_0(u, v) = f(v), \text{ for all } v \in H^1(\Omega_0), \quad (3.13)$$

where

$$\begin{aligned} \Phi_0(u, v) &= \int_{\Omega_0} \nabla u^T \bar{\bar{A}}(\vec{x}) \nabla v \, d\vec{x} - k_0^2 \int_{\Omega_0} b(\vec{x}) uv \, d\vec{x} \\ f(v) &= \int_{\Omega_{sc}} \left(1 - \frac{\epsilon_{lay}}{\epsilon_{sc}}\right) k_0^2 u^{inc} v \, d\vec{x} + \int_{\Gamma} (\epsilon_{lay}^{-1} - \epsilon_{sc}^{-1}) \partial_n u^{inc} v \, ds, \end{aligned}$$

and

$$\begin{aligned} \overline{\overline{\mathbf{A}}}(\vec{x}) &= \begin{pmatrix} \frac{\gamma_y(y)}{\gamma_x(x)} \frac{1}{\epsilon(\vec{x})} & 0 \\ 0 & \frac{\gamma_x(x)}{\gamma_y(y)} \frac{1}{\epsilon(\vec{x})} \end{pmatrix} \\ b(\vec{x}) &= \gamma_x(x)\gamma_y(y) \\ \gamma_x(x) &= 1 + i\sigma_x(x)/\omega \\ \gamma_y(y) &= 1 + i\sigma_y(y)/\omega \\ \sigma_x(x) &= \begin{cases} 0, & \text{if } |x - x_0| - x_d \leq 0, \\ S_x (|x - x_0| - x_d)^{\alpha_x}, & \text{if } |x - x_0| - x_d > 0, \end{cases} \\ \sigma_y(y) &= \begin{cases} 0, & \text{if } |y - y_0| - y_d \leq 0, \\ S_y (|y - y_0| - y_d)^{\alpha_y}, & \text{if } |y - y_0| - y_d > 0. \end{cases} \end{aligned}$$

Note that the boundary term $\int_{\partial\Omega} \frac{1}{\epsilon(\vec{x})} \partial_n u v \, ds$ disappears due to the continuity at the PML interface $\partial\Omega$.

In the formulation, (x_0, y_0) is the center of the computational domain, and x_d, y_d are the distances of the PMLs from the center in x and y directions. The geometrical configuration of the PML is shown in Figure 3.14. The functions σ_x and σ_y describe the profile of the PML. They are monotonic polynomial functions in x and y inside the PML region, where the constants S_x, S_y are the amplitudes and α_x, α_y are the polynomial orders of the profiles. The profiles play a key role for the performance of PML. It is nowadays accepted that the profile functions σ_x and σ_x should be continuous over the PML interface, which leads to the continuity of the first derivative of u , as well as their first derivative such that the second derivative of u is continuous as well. Hence, we choose $\alpha_x, \alpha_y \geq 2$.

Furthermore, the combinations of S_x, S_y and α_x, α_y must be chosen carefully. Greater S_x, S_y provides better absorption and decreases the modeling error, but also leads to more rapid decay of the field in the PML, and needs more effort for the discretization. The stronger the PML absorption, the more computational effort is required.

CONCEPTs implementation

For the discretization of (3.13), we use the C++ library **CONCEPTs** [79, 16, 13]. The **CONCEPTs** package uses high polynomial basis functions and curved quadrilateral elements. In **CONCEPTs** the polynomial order can be chosen independently

in each cell. Hence, we can use the library for adaptivity in the mesh width as well as the polynomial order. All the integrals in the formulation can be implemented in **CONCEPTs**, and the corresponding relationships are shown in Table A.2.

integral	CONCEPTs class	symbol	type
$\int_{\Omega} \nabla u^T \bar{\bar{A}}(\bar{x}) \nabla v \, d\bar{x}$	hp2D::Laplace	\mathcal{S}	stiffness matrix
$\int_{\Omega} b(\bar{x}) uv \, d\bar{x}$	hp2D::Identity	\mathcal{M}	mass matrix
$\int_{\Gamma} f v \, ds$	hp1D::Riesz	f_{Γ}	load vector
$\int_{\Omega_{sc}} g v \, d\bar{x}$	hp2D::Riesz	$f_{\Omega_{sc}}$	load vector

Table 3.2: The implementation of the integrals in **CONCEPTs**

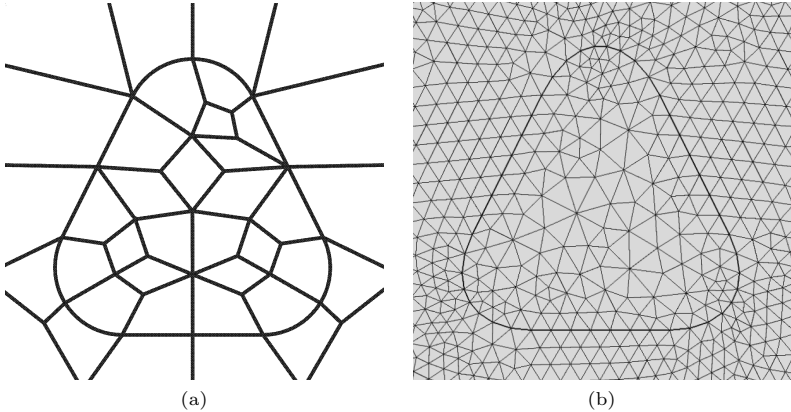


Figure 3.15: **CONCEPTs** and **COMSOL** meshes near the scatterer. (a) The **CONCEPTs** mesh using quadrilateral elements generated by EZ4U. (b) The **COMSOL** mesh using triangular elements.

CONCEPTs requires quadrilateral curvilinear elements. For obtaining an appro-

appropriate mesh of the structure, we applied the mesh generator EZ4U [80, 37] for a small rectangular box including the scatterer, which generates quadrilateral curvilinear elements with good quality, as shown in Figure 3.15(a). This mesh describes the details of the curved scatterer. For FEM based straight triangular or quadrilateral cells a fine mesh is required, to resolve the material interface with curved elements, we may use coarse cells as the circular curved obstacle is exactly resolved by the mesh.

3.3.2 Numerical simulations

We aim to apply the introduced FEM formulation with PML to two examples and to verify the accuracy of the simulation by a comparison with results using a MMP code with multilayer Green's functions. To show the efficiency of using high-order finite elements for multilayer scattering problems using PML we compare our implementation in the high-order FEM library `CONCEPTs` with the commercial FEM program `COMSOL`.

Test problems

As shown in Figure 3.14, we compute the scattering of a plane wave at a silver scatterer that is embedded in a three-layer medium. All the layers extend towards infinity in horizontal direction. The center layer, with thickness 350 nm and relative permittivity ϵ_{lay} , is coated with two 50 nm-thick layers with relative permittivity ϵ_{coat} . A TE-polarized plane wave is impinging from top with 45 degrees angle of incidence. The wavelength of the plane wave is 600 nm, at which the relative permittivity of silver ϵ_{Ag} is $-15.855+0.432i$ [27]. With certain combinations of ϵ_{lay} and ϵ_{coat} , guided wave modes can be excited in the coating layers. As our test problem, we choose the relative permittivities $\epsilon_{\text{lay}} = 4$ and $\epsilon_{\text{coat}} = 9$. It should be noted that the geometry analyzed here has three guided waves observed for TE polarization, with the following wave numbers: $k_{gw1} = 1.21k_0$, $k_{gw2} = 1.77k_0$ and $k_{gw3} = 1.97k_0$, where $k_0 = \frac{\omega}{c}$ is the wave number in vacuum.

We simulate two shapes of scatterers. One is a disk of radius 100 nm, another is an isosceles triangle with bottom length of 160 nm and height of 160 nm. The triangle has rounded corners with radii of 30 nm, which is shown in Figure 3.15. Both scatterers are embedded in the middle of the center layer.

Modeling parameters and numerical results

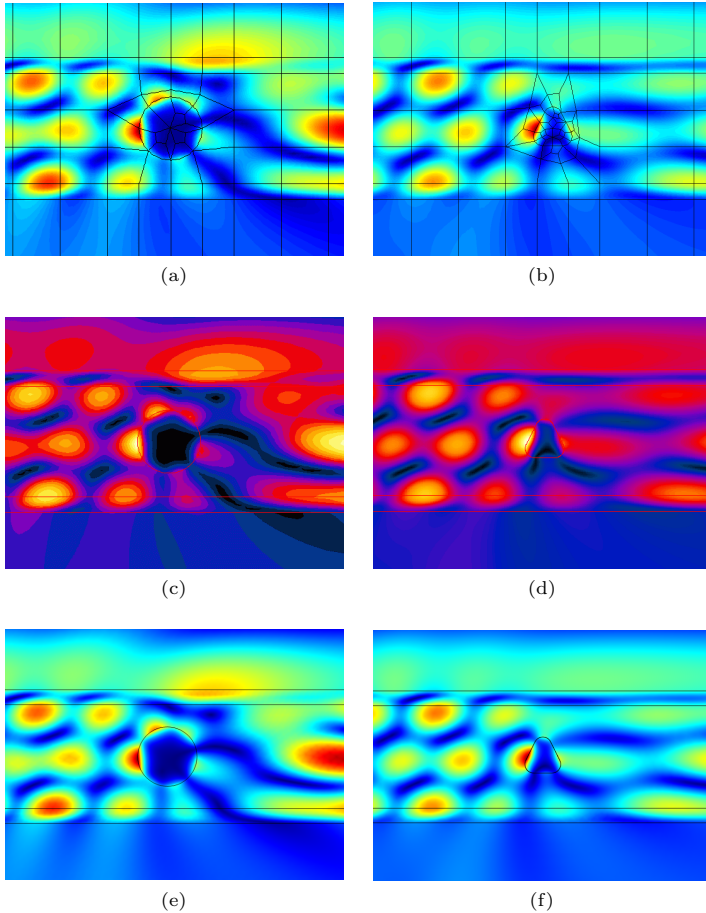


Figure 3.16: Simulation results for the absolute value of the total magnetic field.

In (a),(c) and (e) the results for circular scatterer are shown, and (b),(d) and (f) the results for triangular scatterer. The results with **CONCEPTs** are in (a),(b), where we use a polynomial degree of 14 resulting in 22741 DOFs for the disk, and 21876 DOFs for the triangle. (c),(d) show the MMP results. For the disk, 64 layered expansions and a Bessel expansion with the maximum order of 30 are used. For the triangle, 51 multilayer expansions are used inside the scatterer and 23 homogeneous media multipoles are used outside the scatter. (e),(f) **COMSOL** results using quadratic elements, where 155798 DOFs are used for the disk and 177477 DOFs for the triangle.

For the simulations with the proposed formulation and using **CONCEPTs** we choose as domain of interest the box with $x_d = 800$ nm and $y_d = 550$ nm and add a PML layer of 100 nm thickness in both x and y direction around. The PML profiles are parabolic curves with parameters $S_x = S_y = 0.2$, and $\alpha_x = \alpha_y = 2$.

Coarse meshes around the scatterers are generated by **EZ4U**. This mesh has 27 cells for the disk and 49 cells for the triangle (see Figure 3.15(a)). For the multilayers and PML layer a Cartesian mesh is added to obtain combined mesh with 191 cells for the disk and with 205 cells for the triangle. We use a uniform polynomial degree of 14 resulting in 22741 DOFs for the circular scatterer and 21876 DOFs for the triangular one. The absolute values of the total magnetic fields are shown in Figure 3.16(a) for the disk and in Figure 3.16(b) for the triangle. The excited guided waves are observed in the layers. With the used simulation parameters, one observes almost no artificial reflection by the PML layer. The PML performs very well when truncating the layers containing strong guided waves.

To verify the simulation with the proposed formulation, **OpenMaXwell**, an open source electromagnetic simulation tool that includes the Multiple Multipole Program (**MMP**) is used. **MMP** is a boundary discretization method that uses a set of fundamental solutions of Maxwell's equations (multipole expansions) in order to obtain the fields scattered by objects [17, 18, 19, 20]. Inside the scatterer an expansion with Bessel functions or multipoles of different centers is used, whereas in the multiple layers the solution is expanded in multilayer Green's functions with different centers. For the circular scatterer 64 multilayer Green's functions and a Bessel expansion with the maximum order of 30 are used. Solutions are obtained with the average field mismatch error criterion of 0.001% checked in 256 matching points distributed linearly on the scatterer. For the triangular scatterer, 51 multilayer Green's functions and 23 homogeneous media multipoles with the maximum order 3 are used. The problem is solved by using 150 matching points with the average mismatch error of 0.02%. The absolute values of the total magnetic fields are shown in Figure 3.16c for the disk and in Figure 3.16d for the triangle.

We also simulated the test problem with **COMSOL** Multiphysics version 4.3a [36]. Under the graphical interface of **COMSOL**, linear, quadratic and cubic elements are available, which correspond to the 1st, 2nd and 3rd order elements, respectively. We choose quadratic and cubic elements for computation. The geometrical approximation is chosen to be 'Quintic' (5th order). Since the polynomial orders two and three are rather low, we choose a much finer mesh (see Figure 3.15(b)) with 16288 cells for the disk for $p = 2$, and 7172 cells for $p = 3$, while with 9506 cells for the triangle for both $p = 2$ and $p = 3$. For the circular scatterer, the simulation consumes 155798 DOFs when using quadratic elements. In the simulation using cubic elements, for which a coarser mesh is applied, 141791

DOFs are consumed. For the triangular scatterer, the simulations consume 177477 DOFs when using quadratic elements and 229827 DOFs when using cubic elements. Finally, the PML is configured by the default settings. The absolute values of the total magnetic fields for the performed simulations are shown in Figure 3.16e for the disk and in Figure 3.16f for the triangle, where both of the simulations use quadratic elements.

Comparisons

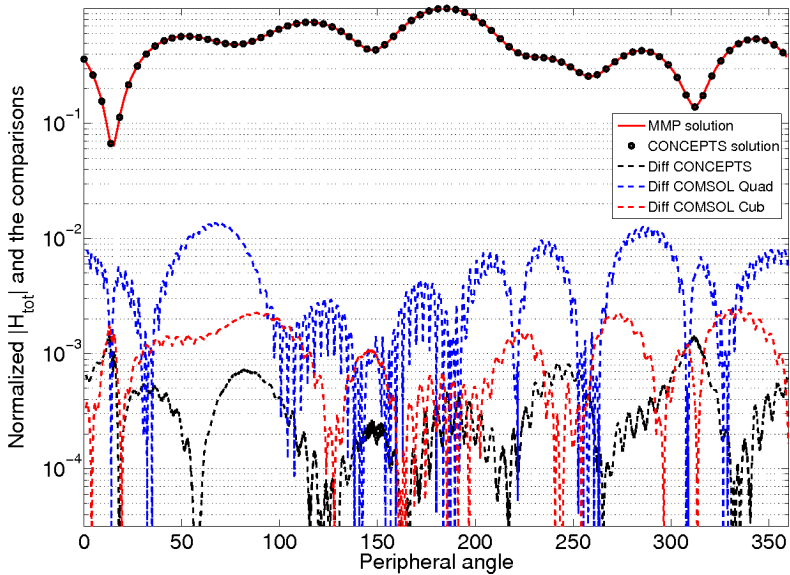


Figure 3.17: Comparisons for the normalized absolute value of the total magnetic field along the trace of the silver disk Γ (in logarithmic scale). The red curve represents the MMP result. The black dots represent the CONCEPTs result. The black dashed curve represents the difference between CONCEPTs and MMP results; the blue dashed curve represents the difference between MMP result and COMSOL result using quadratic elements, and the red dashed curve represents the difference between MMP result and COMSOL result using cubic elements.

We compare the accuracy of the simulations with **CONCEPTs** and **COMSOL** in terms of the normalized absolute value of the total magnetic field $|H_{\text{tot}}|/\max(|H_{\text{tot}}|)$ along the interface of the silver disk Γ . For MMP it is known that the accuracy is of the order of the field mismatch about 10^{-5} . Hence, we use the result obtained with MMP as reference. The computed fields and the differences of the **CONCEPTs** solution, the **COMSOL** solutions using quadratic and cubic elements to the reference solutions are shown in Figure 3.17. We obtain maximal errors of 1.5×10^{-3} for the **CONCEPTs** solution, and 1.4×10^{-2} and 2.4×10^{-3} for the **COMSOL** solutions with quadratic and cubic elements, respectively.

From the comparison, one can see the advantage of using high order elements. Compared to the quadratic elements, the cubic elements use a coarser mesh and less DOFs, while they achieve even higher accuracy. **CONCEPTs** simulation using polynomial degree 14 uses an even coarser mesh and much less DOFs, where an even higher accuracy is achieved. From the comparison, one can draw the conclusion that high order FEM is more efficient than low order FEM for our problem.

3.3.3 hp-FEM analysis

Finite element methods are based on piecewise polynomial approximations of the solution of a partial differential equation, which is based on a partition of the computational domain in curvilinear cells. The accuracy of the solution can be improved either by h -refinement, or by p -refinement, or by a combination of both, hp -refinement [40]. We speak about hp -adaptive FEM [40] for refinement strategies where each cell may be refined independently and the polynomial order in each cell may be raised independently.

For the studied formulation with PML, the solution in the domain of interest Ω and in the PML layer Ω_{PML} have different properties. We study the test example of a silver disk which was described in Section 3.3.2, for which we start with a coarse mesh resolving the scatterer, the interfaces of the multiple layers and the PML interface.

For this example, the solution is primarily smooth in each subdomain of different material in the physical domain Ω . Therefore, we apply only uniform p -refinement in Ω and call p_{int} the polynomial order in these cells. For the given mesh, the polynomial order has to exceed a particular value such that the wave form can be at least coarsely resolved and the solution converges [53, 81, 82].

The complex coordinate transformation of PML leads to exponentially decaying solutions inside the PML layer, which results in very high gradients close to the PML interface, while vanishing close to the outer boundary. This behavior of the solution may lead to a locking phenomenon when using a uniform mesh refinement, that means a convergence of the solution may start only for a very small mesh width. This phenomenon is weakened by using continuous profile

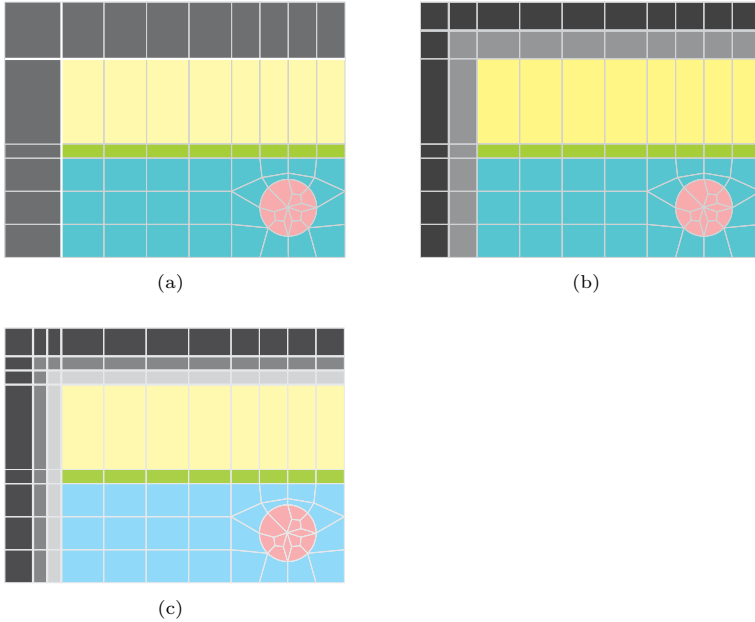
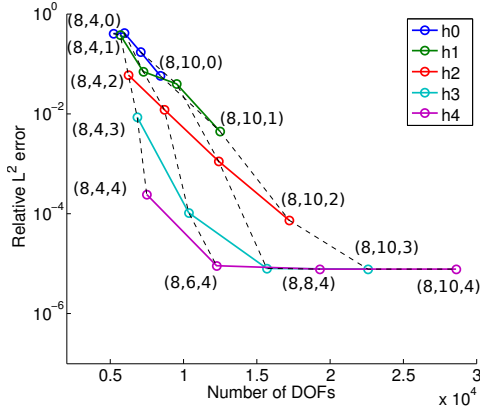


Figure 3.18: Adaptive h -refinement. (a) the original mesh h_0 . (b) mesh h_1 , obtained by one step of h -refinement from mesh h_0 . (c) mesh h_2 , obtained by one more step of h -refinement from mesh h_1 .

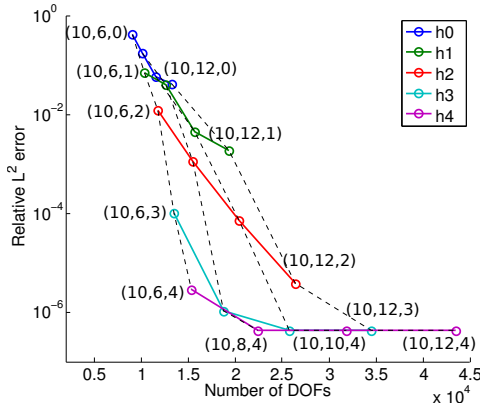
functions and optimized PML parameters. Motivated by the exponentially decaying solution we are going to study a geometric mesh refinement towards the PML interface. Figure 3.18 illustrates this refinement strategy. The mesh in Figure 3.18(a) is the original mesh, which we call h_0 . To obtain the refined mesh h_1 (see Figure 3.18(b)) from h_0 we subdivide all cells having one edge on the PML interface or its extension in the respective outer direction. In the same way mesh h_2 (see Figure 3.18(c)) is obtained by another geometric refinement of mesh h_1 . In general we have a mesh h_ℓ , $\ell \in \mathbb{N}$.

The study of this mesh refinement will be in comparison to a uniform p -refinement in the PML layer, which is motivated by the fact that the decaying solution is piecewise smooth. We call p_{ext} the polynomial order of the cells in the PML layer, which may be different from p_{int} .

Hence, we characterize the hp -adaptive FEM strategy as an array of numbers $(p_{\text{int}}, p_{\text{ext}}, \ell)$. For example, $(10, 8, 2)$ means the polynomial degrees are 10



(a)



(b)

Figure 3.19: The hp -convergence analysis for the scattering problem of a silver disk. Each node represents a simulation with an hp combination of $(p_{\text{int}}, p_{\text{ext}}, \ell)$. (a) A group of 20 simulations with $p_{\text{int}} = 8$, $p_{\text{ext}} \in [4, 6, 8, 10]$, and $\ell \in [0, 1, 2, 3, 4]$, (b) A group of simulations with $p_{\text{int}} = 10$, $p_{\text{ext}} \in [6, 8, 10, 12]$, and $\ell \in [0, 1, 2, 3, 4]$. The solid lines connect the nodes with the same mesh and show the convergence with respect to p_{ext} . And the dashed lines connect the nodes with the same p_{ext} and show the convergence with respect to the mesh refinement.

in the physical domain and 8 in the external PML domain, and two steps of h -refinement are applied in the PML domain towards the PML interface.

We start the study with $p_{\text{int}} = 8$ and $p_{\text{ext}} = 4$ on the coarse mesh h_0 , for which the relative L^2 error in the domain of interest is below 1. The relative L^2 error is defined as the ratio between the L^2 norm of the discretization error $u_{hp} - u_{\text{ref}}$ and the reference solution u_{ref} in the domain of interest, which reads

$$\frac{\sqrt{\int_{\Omega} |u_{hp} - u_{\text{ref}}|^2 d\vec{x}}}{\sqrt{\int_{\Omega} |u_{\text{ref}}|^2 d\vec{x}}}.$$

As reference solution we use a very fine **CONCEPTs** solution with an hp combination (24, 24, 4). For fixed $p_{\text{int}} = 8$ we vary p_{ext} and ℓ from a combination of $[4, 6, 8, 10] \times [0, 1, 2, 3, 4]$. For each instance of the simulation, we compute the relative L^2 error and record the degrees of freedom. To see also the influence of p -refinement in the physical domain we repeat a similar set of simulations with $p_{\text{int}} = 10$ and a combination of p_{ext} and ℓ in $[6, 8, 10, 12] \times [0, 1, 2, 3, 4]$. The results of the convergence study are illustrated in Figure 3.19, where the first group of simulations is shown in Figure 3.19(a), while the second group is shown in Figure 3.19(b). In each figure, there are 20 points obtained from 20 instances of FEM simulations. We connect the points with the same h -refinement by solid lines, while the points with the same p_{ext} by dashed lines. The solid lines represent the p -convergence of p_{ext} , while the dashed lines represent the adaptive h -convergence.

One observes in both diagrams that the error decays if either p_{ext} is increased or the mesh refinement towards the PML interface, until a saturation level is reached, where further refinement inside the PML layer has no effect on the error. For $p_{\text{int}} = 8$ the relative error can be reduced to 9.00×10^{-6} which is reached for the hp combination (8,6,4) and with 12259 DOFs. When the saturation level is approached, the error inside the physical domain becomes dominant and further error reduction is only possible by increasing p_{int} . By increasing p_{int} from 8 to 10 the level of error saturation reduces by a factor of 20. An relative L^2 error of 4.16×10^{-7} is obtained for the hp combination (10,8,4) with 22465 DOFs. Before the saturation level is reached, the error inside the PML domain dominates, therefore hp -refinement in the PML domain will lead to convergence to the exact solution. We observe exponential convergence above the saturation level both for p -refinement in the PML layer and the adaptive mesh refinement, whereas the mesh refinement towards the PML interface is computationally more efficient than increasing p_{ext} — the dashed lines in Figure 3.19 are more steep than the solid lines. We observe that mesh refinement towards the PML interface is more adapted to the exponential decay of the solution inside the PML layer than increasing polynomial orders. For instance, starting with the hp

combination (8,4,0), an error level of about 10^{-4} is reached by four steps of the adaptive mesh refinement, *i. e.*, at (8,4,4), with 7503 DOFs, whereas increasing the polynomial degree p_{ext} to 10 only leads to an error of about 6×10^{-2} with 8432 DOFs at (8,10,0). If we start increasing p_{ext} from hp combination (8,4,2), *i. e.*, after two steps of mesh refinement from (8,4,0), the error drops below 10^{-4} at hp combination (8,10,2), with 17243 DOFs, which is more than two times that for the hp combination (8,4,4). Nevertheless, we expect that it is necessary to increase p_{ext} to obtain very low error levels. It should also be noted that if the mesh is too coarse and the polynomial orders are too low, there is no error reduction by mesh refinement or by increasing the polynomial degree. For example, we also observed in our experiments that the error does not decrease when we start with (8,4,0), no matter if p_{ext} is increased to 6 or one step of the adaptive mesh refinement is applied. This is due to the fact that the hp combination is not entering the asymptotic regime of convergence.

Having many numerical solutions with their different hp combinations computed, we can answer the question of optimal refinement strategies for this example, which is assumed to also hold for similar problems. We assume three refinement options:

- a. increasing p_{int} by 2,
- b. increasing p_{ext} by 2, and
- c. one step of adaptive mesh refinement, so increasing ℓ by 1.

To expose an optimal strategy we start with an hp combination (8,6,0), which is in the asymptotic regime of convergence. Then, we compare the error reductions for the three options, and choose the one with the highest error reduction for least increase of degrees of freedom and repeat the steps for this choice. In Figure 3.20 the optimal refinement strategy is illustrated. For the starting combination (8,6,0) with 5979 DOFs an relative error of 4.05×10^{-1} is obtained. Option c is the best choice for the first four steps, therefore four h -refinement steps are performed and lead to the hp combination (8,6,4). In the fifth step, the saturation is reached, therefore neither option b nor c will improve the solution anymore, however, option a will surpass the saturation level of p_{int} and leads to a further improvement. Therefore option a is applied and the strategy ends at the hp combination (10,6,4) with 15389 DOFs and an error of 2.83×10^{-6} . At each step, the best choice is plotted as solid line, while the unchosen ones as dashed lines. All the steps generate a decision tree, where each node represents the optimal choice in each step, whereas dashed branches show the non-optimal choices.

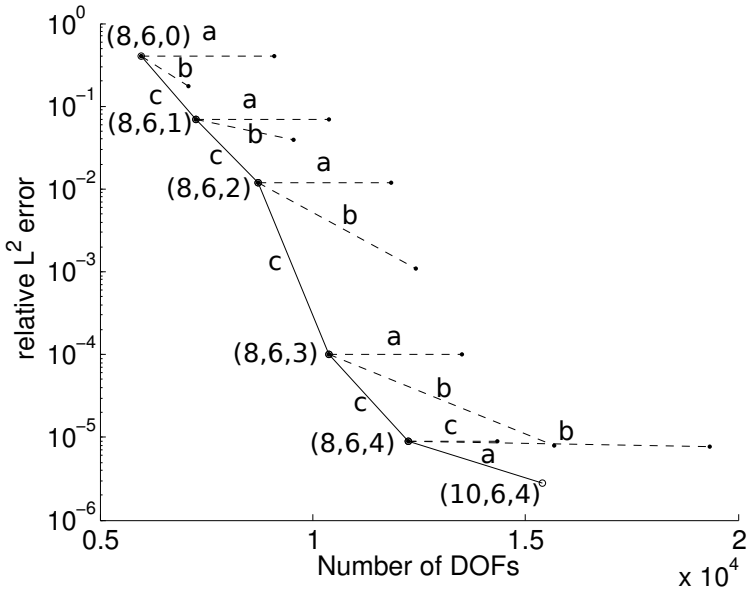


Figure 3.20: The hp -convergence strategy. Three options are represented by a,b, and c, where a means increasing p_{int} by 2, b means increasing p_{ext} by 2, and c means increasing ℓ by 1. The experiment starts at the hp combination $(8,6,0)$ with 5999 DOFs and an error of 4.05×10^{-1} , and stops at the hp combination $(10,6,4)$ with 15389 DOFs and an error of 2.83×10^{-6} .

3.4 Summary

We formulated ABC and PML with FEM, and implemented them using the FEM package `CONCEPTs`. For ABC, we implemented the 0th to 2nd BGT conditions, and found that their performances are limited by the distance between the scatterer. BGT conditions were derived based on an asymptotic expansion in $k_0 R$, as a result, there is a limitation of the model for a fixed domain size. The closer the boundary is placed, the faster the convergence of p -FEM. However, the model error of the BGT condition increases when the artificial boundary is put closer to the cylinder(s), which finally dominates the overall error.

For PML, we observed that the PML performs very well even in the presence of strong guided waves inside the layers. We also learned that there is a saturation level of error for PML. When the saturation level is reached, one can only reduce it further by increasing the polynomial degrees in the physical domain. This phenomenon shows that the saturation level is decided by the modeling error inside the physical domain.

For both ABC and PML, convergence analyses were performed. For ABC, we compared the p -FEM to h -refinement with polynomial degree 2. We observed much faster convergence with the p -refinement. For PML, the solution is exponentially decaying inside the PML domain, therefore adaptive mesh refinement inside the PML region gives better convergence. Based on these discoveries, an hp strategy is developed for PML, and it converges to very high accuracy within very few steps and with a small additional cost of DOFs.

4 Numerical optimizations

4.1 Introduction

Optical nano antennas are currently promising key elements for sensing and optical communication [83, 84, 2, 85]. However, they exhibit considerable difficulties because of plasmonic resonances that occur in the optical regime.

Traditional RF antennas essentially are scalable, *i. e.*, their resonance wavelengths are proportional to the antenna size, which allows one to derive rather simple engineering formulas for the design of such antennas [56, 86]. In contrast to this, plasmonic nano antennas may resonate even when they are much smaller than the wavelength. Their bandwidth in the optical range is often broader than required. Although the geometry has a strong impact on resonances and on the antenna performance, the bandwidth is mostly caused by the rather high losses in metals at optical frequencies. As a result, plasmonic nano antennas are not scalable, their quality factor is usually not very high, and it is very hard or even impossible to find simple design rules.

Currently, the most promising approach to designing plasmonic nano antennas for a specific application is to benefit from appropriate combinations of numerical optimizers with simulation tools for electromagnetics that may efficiently simulate plasmonic structures [87]. In the last few years, many numerical optimizations methods have been developed and several numerical optimizers have been embedded in various commercial simulation tools, such as COMSOL Multiphysics [36].

The main issues are the following: 1) In order to achieve acceptable simulation accuracy, the simulation time of a single plasmonic structure may be rather long. 2) Working on massively parallel computers may become extremely expensive because of high license costs of commercial software. Therefore, one might prefer using some freely available simulation tool which is typically less user-friendly than a commercial one. 3) The optimizer will usually design many different structures. Some of them may look rather complicated. Despite of this, the solver should not fail and return a reasonable result, *i. e.*, the solver must be completely automatic and robust without any support by the user. 4) Inaccuracies of the solver may disturb the numerical optimizer considerably. This especially holds for deterministic optimizers that approximate the gradient information in the parameter search space as soon as they are in the vicinity of an optimum. As a consequence, techniques to speed up the simulation tool by reducing its accuracy may drastically increase the overall cost of the opti-

mization. 5) The overall computation time can become extremely long and depends heavily on the collaboration of the simulation tool with the optimizer. 6) Without any prior knowledge on the complexity of the optimization problem (smoothness of the fitness landscape in the search space, number and shape of local optima, etc.), it is impossible to select an appropriate optimizer. 7) Obtaining information on the complexity of the optimization problem may be hard - especially when the search space is high-dimensional - because even small parts of plasmonic structures may have a considerable impact on the solution.

In this chapter, we study two examples of two-dimensional plasmonic waveguide couplers for exciting a guided wave in a dielectric slab in order to illustrate the various difficulties mentioned above. The first example is a coupler consisting of only two circular metallic particles, which leads to five optimization parameters. And the second example is the unidirectional coupler [88], where dipolar antennas act as the couplers. This example only has three optimization parameters, but some numerical problems make it rather complicated. Note that this structure was used in [88] to launch plasmons. In this thesis, we use it for exciting a dielectric waveguide mode.¹

4.2 Numerical optimizers

In the design of geometric structures, one often faces high-dimensional optimization problems that may only be tackled numerically. Usually, a real-valued fitness function or cost function is defined and the optimizer has to locate local or global maxima of the fitness function or minima of the cost function. Whether one prefers working with fitness or cost functions is not relevant. In all demanding cases, the optimization problem is non-linear and an iterative search has to be performed. This search may be subject to additional constraints.

For a long time, mathematicians were focusing on various deterministic algorithms for non-linear optimization in high-dimensional parameter search spaces [89]. These algorithms are very mature and efficient when either the starting point of the search is close to the desired optimum or when the optimization problem is simple enough. Many of these algorithms require gradient information or even second order derivatives of the fitness function, which is usually not available when the fitness is calculated from a numerical solver as in our examples. Therefore, only deterministic optimizers without gradient information are useful for most of the engineering applications. A prominent example of a deterministic optimizer without gradient information is the Nelder-Mead algorithm that is also known as downhill simplex method [90]. This algorithm is efficient when the number of dimensions of the parameter search space is rather low, and when there are not many local optima within the search space.

¹This part was essentially published in [9]

In our first test example, Nelder-Mead could be applied, if we knew that there is only one optimum in the search space, or if we could approximately guess its location. In the case of plasmonic waveguide couplers, it is clear that there must be several local optima. For the simple structure with only two plasmonic particles, one can estimate the optimal distance between the particles from the wavelength of the mode that shall be excited.

If one is unsure about the problem complexity, one may benefit from an optimization strategy that is not purely deterministic and includes some randomness. Such optimizers have been studied intensively in the second half of the 20th century. Many of them are inspired by optimization processes that seem to be ongoing in physics and nature. An excellent overview may be found in [91].

Currently, the most widely applied nature-inspired algorithms in engineering are probably genetic algorithms (GAs) [92, 91]. These algorithms mimic the evolution of animals (and plants), where the genotype (genetic material in the chromosomes, the genetic code) is separated from the phenotype (the visible properties of the animal). The genotype of a GA is typically a bit string, but the binary basis can be replaced easily by some other basis. The phenotype in the case of an N-dimensional parameter optimization problem is simply a point in the search space, *i. e.*, an N-dimensional vector containing the N optimization parameters. In order to map the genotype, *e. g.*, the bit string, on the phenotype, some decoding routine must be provided by the user of the GA. Since this is not unique at all, a good choice of the decoding is highly important for the GA performance, which is often not simple. As a result, standard GAs are usually outperformed by Evolution Strategies (ESs) [93, 91], which are closely related to GAs without using the genotype-phenotype scheme with its requirement for coding-decoding. In an ES, the individual is directly characterized by its N-dimensional parameter vector (the phenotype) and usually, by a variation vector that is also N-dimensional in typical ES implementations. The variation vector indicates how much mutation may modify the individual. Beside these differences both GAs and ESs work with populations of some individuals. They select the best ones as parents for children of the next generation, create the children by crossover of typically two parents followed by mutation with some probability, and discard the least fit individuals.

For our optimization problems (see section 4.3), we apply a standard $(\mu + \lambda)$ ES with the number of parents $\mu = 5$ and the number of children $\lambda = 7\mu$. The factor 7 is known to be a reasonable choice for standard ES. This algorithm can be downloaded from [94].

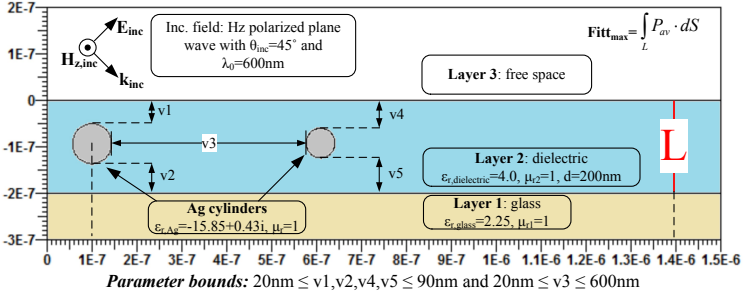


Figure 4.1: The geometrical configuration of the test problem. The dielectric waveguide with permittivity 4.0 is placed in between the glass and air. Two silver cylinders are embedded in the waveguide. The structure is excited by an H_z polarized plane wave with 600 nm wavelength. The location of the cylinders is characterized by $\bar{V} = \{v_1, v_2, v_3, v_4, v_5\}$, which are the parameters of the optimization problem.

4.3 Test problems

Our goal is to optimize the performance of 2D plasmon-assisted waveguide couplers, having the maximum power coupled into the waveguide. With the help of plasmonic structures, the power can feed into the waveguide [2, 85].

Test problem 1

The first test problem is shown in Figure 4.1, where a dielectric waveguide with permittivity 4.0 is mounted on a glass substrate with permittivity 2.25, and the region above is free space. An H_z polarized planewave with 600 nm wavelength is impinging from top-left at an angle of 45 degrees. Two silver cylinders are embedded in the waveguide. At 600 nm, the permittivity of silver is $-15.855 + 0.432i$ [27] and the cylinders behave as a plasmonic coupler. The thickness of the waveguide is 200 nm, and for the left cylinder, the distances between the upper and lower interface of the waveguide are v_1 and v_2 , and for the right cylinder v_4 and v_5 . The horizontal distance between the two cylinders is v_3 .

In order to optimize the power coupled into the waveguide, we place an observer interface L , which is 1300 nm away from the center of the left cylinder.

One can choose the power flux through L as the fitness function F .

$$F = \int_L P^{AV} dl.$$

In order to compare the results among different methods, we define the normalized fitness function \hat{F} as follows. We determine the best parameters among all methods, and compute the best fitness F_{\max} using these parameters. Then we normalize the fitness function with F_{\max} . The normalized fitness function \hat{F} reads

$$\hat{F} = \frac{\int_L P^{AV} dl}{F_{\max}}.$$

The way of selecting the geometrical parameters may seem a bit unnatural at the first glance, however, it works very well with the optimizer. The greatest advantage is that all the five parameters do not interfere with each other. If one would select the radii of the cylinders as the parameters, some additional constraints would have to be applied in order to avoid the cylinders to touch the substrates or to collide. Secondly, it is rather simple to map the data into the normalized range $[0,1]$, which fits the standard data interface for our optimizer.

In our experiments, $\bar{V} = \{v_1, v_2, v_3, v_4, v_5\}$ represents the data set with $v_1, v_2, v_4, v_5 \in [20, 90]$ nm, and $v_3 \in [20, 600]$ nm. For the numerical optimizer, we normalize these parameters by linear mapping on $\bar{P} = \{p_1, p_2, p_3, p_4, p_5\}$, with $p_1, p_2, p_3, p_4, p_5 \in [0, 1]$. Hence, the mapping between the two sets is

$$\begin{aligned} v_i &= (20 + 70p_i) \text{ nm}, i = 1, 2, 4, 5 \\ v_3 &= (20 + 580p_3) \text{ nm}, \end{aligned}$$

which represents a 5-dimensional optimization problem with a standard parameter set \bar{P} .

Test problem 2

The second test problem, as shown in figure 4.2, has the same configuration of a waveguide as in the first one, but the coupling elements are two identical silver rods on top of the waveguide. These rods behave as dipolar antennas [88]. This configuration is motivated by the observation in the first test problem that the fitness is improved when the silver cylinders are moved towards the air-glass interface. With the selection of zero distances of the cylinder from the interface, two optimization parameters disappear. By replacing the circular shape by an rectangular shape, sharp corners and triple points occur, which provide additional numerical difficulties. There are totally three optimization parameters, the width of the rods l , the height of the rods h , and the distance between the rods d .

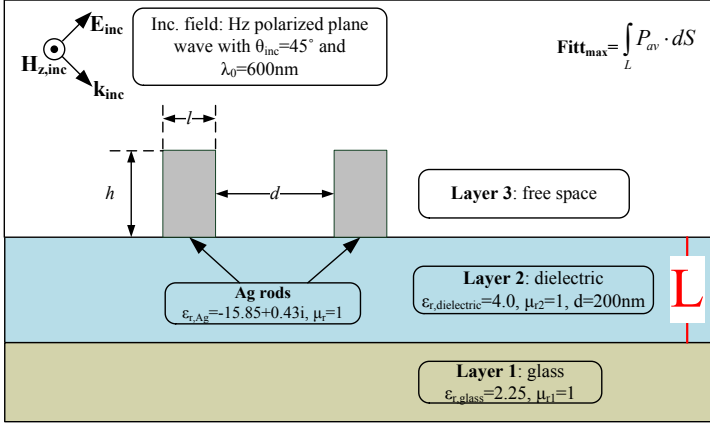


Figure 4.2: The geometrical configuration of the second test problem. The dielectric waveguide with permittivity 4.0 is placed in between the glass and air. Two silver rods are placed on the surface of the waveguide. The structure is excited by an H_z polarized plane wave with 600 nm wavelength. The location of the rods is characterized by l, h, d , which are the parameters of the optimization problem.

To measure the power coupled into the waveguide, we place again an observer interface L inside the waveguide, which is 1800 nm away from the left corner of the left rod, and we define the normalized power flux as the fitness function \hat{F}

$$\hat{F} = \frac{\int_L P^{AV} dl}{F_{\text{max}}},$$

where F_{max} is the best fitness among all optimizations.

Following the procedure of the first example, $\bar{\mathbf{V}} = \{l, d, h\}$ is chosen to represent the data set with $l \in [100, 200]$ nm, $d \in [200, 1200]$ nm and $h \in [200, 400]$ nm. Then the normalized parameter vector $\bar{\mathbf{P}} = \{p_1, p_2, p_3\}$ represents the 3-dimensional optimization problem, with the mapping

$$\begin{aligned} l &= (100 + 100p_1) \text{ nm}, \\ d &= (200 + 1000p_2) \text{ nm}, \\ h &= (200 + 200p_3) \text{ nm}. \end{aligned}$$

Note that for this problem, there can be singularities at the material interfaces, therefore adaptive refinement will be helpful.

4.4 Solvers for plasmonic structures

In computational electromagnetics one may characterize the available numerical methods by the way they handle time and space. This leads to the two categories of time-domain and frequency-domain solvers. Time-domain solves such as FDTD attracted much interest and were also used for plasmonics. However, FDTD requires an extremely fine discretization in space (0.5 nm grids) and time (because of the stability criterion) [95] and suffers from undesired stair-casing effects. Another problem is caused by the fact that metals are strongly dispersive, *i. e.*, their permittivity is strongly frequency-dependent at optical frequencies. To handle this problem, simplified Drude and Lorentz models are usually applied, which introduce additional errors, especially in the area of interest, where the real part of the relative permittivity of the metal is changing its sign. Since we want to avoid errors of the field solvers that might disturb the optimizer, and since we intend to optimize the plasmonic waveguide coupler for a certain frequency, we do not consider time-domain solvers in the following.

Since most of the configurations of interest consist of materials separated by interfaces or boundaries, one may have two categories of space discretization, domain discretization, where the entire space is discretized by some elements of finite size (FEM) or where only the interfaces or boundaries are discretized. When the boundaries are discretized by elements of finite size, the term Boundary Element Method (BEM) is used.

FEM and similar domain discretization methods suffer from the fact that many structures of interest are not finite and need an appropriate truncation, which is typically done by introducing ABCs[96] or PMLs [66] as discussed in Chapter 3. ABCs and PMLs require additional implementation effort and may introduce additional errors, which must be carefully checked when numerical optimizations are being performed. However, since FEM is most widely used, we want to apply it also in the following.

In order to get information on the FEM accuracy, we need an accurate simulation tool, preferably one that is based on a boundary discretization technique. Since the boundary discretization by means of boundary elements may introduce sharp wedges and corners - which may cause numerical problems in plasmonics - we use the multiple multipole program (MMP) [18], which is an element-free boundary discretization technique that is very close to analytic solutions and therefore may be used as a reference. Because of the smoothness of all boundaries in test example 1, MMP has exponential convergence and provides highly accurate results. This is no longer the case in test example 2, since the sharp

corners and triple points lead to field singularities and destroy the MMP convergence. As a result MMP reference solutions for test problem 2 would be very expensive.

It is important to note that something similar to domain truncation by means of ABCs and PMLs is often not required in boundary discretization methods and MMP because the boundaries are usually finite. A typical example is an antenna surrounded by free space. The boundary of such an antenna, *i. e.*, its interface to free space is indeed finite. In our example of an antenna inside a waveguide (for coupling a plane wave into the waveguide), the boundaries of the antenna are finite, but the boundaries of the waveguide are assumed to be infinite since the waveguide is much longer than the wavelength. Consequently, we need some appropriate procedure to discretize such a structure. This will be outlined in section 4.5.

4.5 Simulation methods

4.5.1 Boundary discretization - MMP

As a reference solution for the first numerical optimization problem, described in Section 4.3, we use MMP together with a genetic optimization algorithm. In order to solve the scattering problem in the given layered medium and calculate the corresponding fitness values for the optimization routine, we use the open source implementation OpenMaXwell [97] of MMP and of layered media Green's functions. By using the automatic expansion distribution routines of OpenMaXwell for the MMP solution, we obtain the results in an efficient and robust way for all the different optimization parameter combinations (the boundary condition mismatch error measured on the scatterers is less than 0.1 percent for the numerical results presented in section 4.6.) For a detailed description of MMP analysis for layered media, refer to [19, 20, 21].

4.5.2 Domain discretization - FEM/CONCEPTs

We choose the C++ library CONCEPTs as our FEM solver, which features high polynomial basis functions and quadrilateral curvilinear elements. Our previous research shows that CONCEPTs with its PML implementation provides high accuracy and efficiency for the problems of plasmonic waveguides. The details can be found in [8].

The ES from [94] is rewritten into MATLAB scripts in order to control the optimization process. For each generation, the ES script generates a new generation, and then passes the parameters to the mesh generator that generates parametric meshes. The applied mesh generator is part of COMSOL Multiphysics. In order to make it parametrically controllable, we link COMSOL with a MATLAB

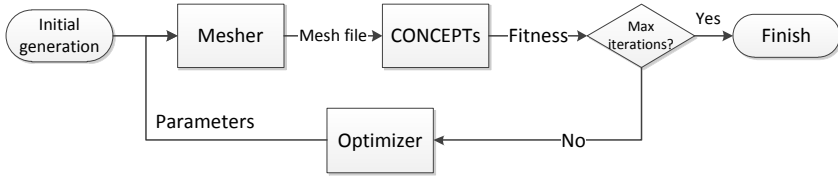


Figure 4.3: The control flow of the optimization. The framework of parametric mesh generation links `CONCEPTs` with `COMSOL`.

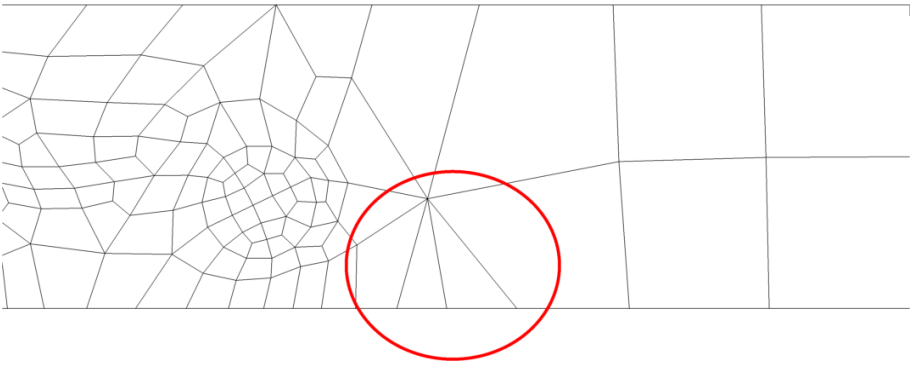


Figure 4.4: `COMSOL` mesh with mixed quadrilateral and triangular elements, which causes problems when solving with `CONCEPTs`. The red circle points out the problematic triangular elements. This problem can be solved by increasing the overall refinement level.

routine with the help of `COMSOL LiveLink for MATLAB`. Then the `CONCEPTs` routine is called to read the parametric meshes and solve the electromagnetic field. Finally, the fitness distribution of the new generation is computed from the `CONCEPTs` results. The process is repeated until the maximum number of iterations is reached. Figure 4.3 shows the control flow of the optimization.

In practice several issues require attention when using meshes as generated by `COMSOL`. Firstly, `CONCEPTs` only works with quadrilateral meshes, however, in some circumstances, `COMSOL` will generate meshes with mixed quadrilateral and triangular elements, as shown in Figure 4.4. Secondly, if there is an element with two adjacent curved edges, as shown in Figure 4.5, the simulation will fail for the following reason. As the plasmonic particles have circular shape, the

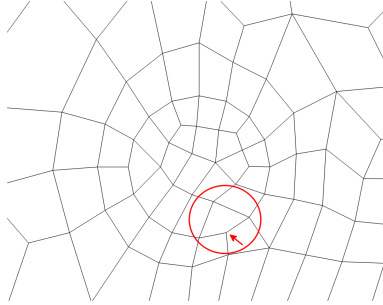


Figure 4.5: COMSOL elements with neighboring curved edges, which causes problems when solving with **CONCEPTs**. The red circle points out one of the problematic elements. This problem can be solved by a further refinement of the circular interface. Note that in the illustration, straight-sided elements are displayed as generated by COMSOL. Problems occur only when the elements are subsequently curved leading to coordinate degeneration at the node indicated by the arrow.

incidence angle at the grid node located between the two curved edges is 180 degrees. This leads to a degeneration of the local element coordinates at the node indicated by the arrow.

To overcome these problems, we need to introduce control parameters in the MATLAB COMSOL scripts. For the first problem, in order to control the overall refinement level, we introduce parameter γ_1 , which has the meaning that the minimal size of elements is $20/\gamma_1$ nm. When a triangular element is detected, the script will send requirement to increase γ_1 . The best empirical values for our problem are 1.05 as the starting value and 0.15 as the increment of γ_1 . For the second problem, we introduce the parameter γ_2 to control the refinement level of the circular interface. It is defined in such a way that the minimal size of the element on the circle is $R/2\gamma_2$, where R is the radius of the corresponding cylinder. When an element with two curved edges is detected, the algorithm will send the request to increase γ_2 . The best empirical values for our problem are 1.2 as the starting value and 0.15 as the increment step of γ_2 .

In the **CONCEPTs** simulation, basis functions of polynomial degree up to 7 are used. The polynomial order 7 is a good choice for fast simulations and high accuracy. The computational time varies according to the refinement level of the meshing step. A typical number of degrees of freedom (DOFs) is a few thousand, and a single simulation takes around 6 to 20 seconds, depending on the complexity of the mesh.

4.6 Optimization results

4.6.1 The first test problem

MMP as solver

For the genetic optimization routine, we use the number of parents $\mu = 5$, number of children $\lambda = 35$, the strength of mutation $\sigma = 0.1$, and the strategy of keeping the best five individuals of the current generation, with a maximum number of solver calls of 1000. As a result, we obtained $\bar{V}_{\text{MMP}} = \{20.00, 65.91, 434.64, 20.00, 77.34\}$ nm for the best fitness value. The distribution of the optimization parameters in the search space and the convergence of the fitness value are plotted in Figures 4.6a and 4.6b, respectively. Figure 4.6a shows that the ES converges first to a local optimum. After 300 iterations, it increases the variability and then converges to the global optimum in the search space. Note that this behavior is not always observed, when the ES is restarted. Figure 4.6b shows the distribution of the five normalized parameters $\{p_1, p_2, p_3, p_4, p_5\}$ during the ES search. This plot gives a rough impression of the fitness landscape, especially near the optimum found. As one can see, all p_1 and p_4 values at high fitness levels are close to 0. This indicates that one might find better solutions by allowing smaller values for the corresponding parameters v_1 and v_4 , which are the distances of the cylinders from the top interface. The shape of the envelopes of p_2 and p_5 are rather broad near the optimum. This indicates that fabrication inaccuracies of the corresponding v_2 and v_5 are not affecting the results very strongly. Note that v_2 and v_5 indirectly define the diameters of the cylinders. The sharpest peak can be observed for p_3 , which indicates that the fabrication tolerance for the distance between the cylinders will be rather small.

CONCEPTs as solver

We take the same configuration as of MMP, *i. e.*, $\mu = 5$, and $\lambda = 35$, $\sigma = 0.1$, and keep the best five individuals of the current generation. The optimizations are performed twice, with maximum number of solver calls of 1000 each time. Figure 4.6c, 4.6e show the convergence results, and Figure 4.6d, 4.6f show the distributions of the parameters. As one can see, the ES convergence depends as much on the random initialization of the ES as on the selection of the field solver. The shapes of the envelopes of $\{p_1, p_2, p_3, p_4, p_5\}$ near the optimum are very similar in all cases, indicating that the interpretation in section 4.6.1 is also valid here. The optimization reaches best fitness with $\bar{V}_{\text{CONCEPTs}} = \{20.00, 62.89, 437.63, 20.00, 75.86\}$ nm, which are close to the MMP values. Note that the differences of the maximum fitness values found with the two CONCEPTs runs are around 0.1% and similar differences between

the MMP and **CONCEPTs** solutions may be observed as well. The optimal values of v_1 and v_4 are always 20 nm, *i. e.*, the minimum allowed distances from the top layer. Because of this observation, we will modify the plasmonic coupling elements in test case 2. The variations in the optimal v_2 and v_5 values are around 5%, which supports the finding that rather high fabrication tolerances for v_2 and v_5 are allowed. The more critical parameter v_3 has a variation of less than 1%, which is also in agreement with the interpretation of Figures 4.6b,4.6d,4.6f.

Due to the randomness of the ES, the convergences look somewhat different, even though the optimization parameters are practically the same. The first one is more 'lucky' that its convergence is faster and the distribution is denser compare to the second one. The optimization progress with FEM is also different from the one with MMP, which is also due to the randomness. In order to make sure that the global optimum is found in the search space, one must either increase the number of ES generations or even better restart the ES many times. In this test problem, this seems to be unnecessary because the fitness landscape is very simple.

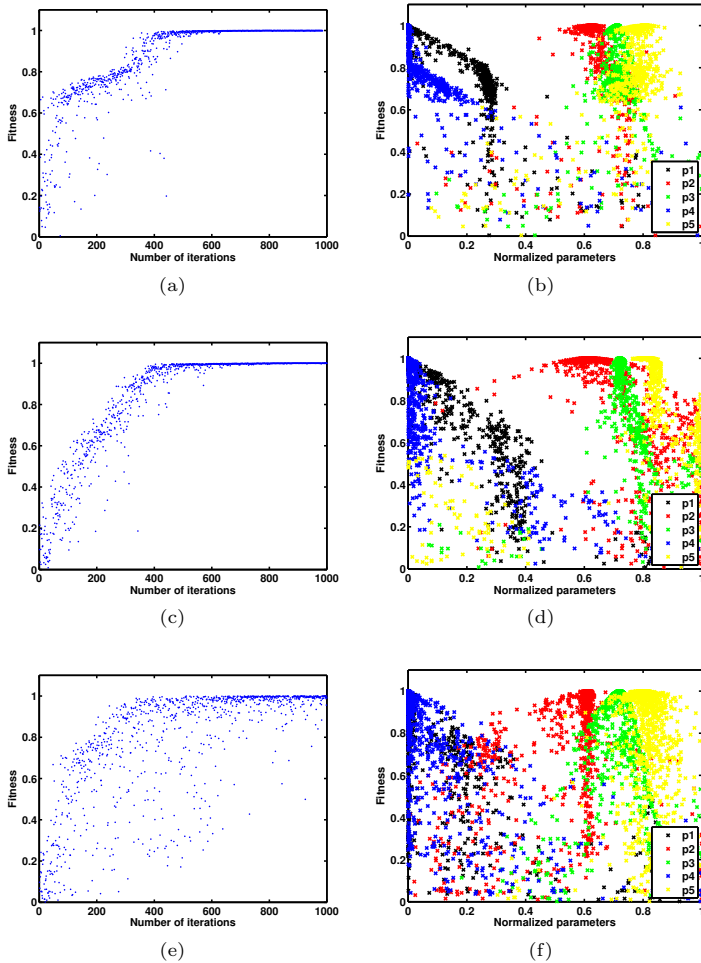


Figure 4.6: The results of the 5-dimensional optimization. The maximum number of individual simulations is 1000, with the number of parents $\mu = 5$, number of children $\lambda = 35$, and strength of mutation $\sigma = 0.1$. p_1 to p_5 are the normalized geometrical parameters, which are mentioned in section 4.3. The strategy keeps the best 5 parent individuals in each generation. (a) shows the convergence with respect to the number of iterations using MMP, and (b) shows the distribution of the normalized parameters versus the fitness function using MMP. (c),(d) are the corresponding results from the first run of CONCEPTs simulation, and (e),(f) are from the second run of CONCEPTs simulation. The optimizations look different each time, only due to the randomness of the optimizer.

Deterministic optimization with COMSOL

Since the fitness landscape seems to be simple, applying a deterministic solver with a good starting point is promising. Therefore, we also used a deterministic optimizer to solve the same 5-dimensional optimization problem, in comparison with the optimization results of ES from section 4.6.1. We used the Nelder-Mead method, which is embedded in the commercial FEM solver **COMSOL Multiphysics** version 4.3b. In the **COMSOL** simulation, we used the default values of the solver (second order shape functions with the largest mesh size set to be less than $1/10$ of the incident wavelength in the corresponding domain) and the built-in Nelder-Mead optimization routine (optimality tolerance of 0.01 and the initial values of the optimization set to be the mid-point of the corresponding parameter bounds). The distribution of the optimization parameters in the search space are plotted in Figure 4.7.

As a deterministic algorithm, Nelder-Mead method requires only 172 instances to converge in this example. However, it works with more strict conditions than ES: the dimension of the optimization should not be very high, and there should not be many local optima within the search space. In order to check the above criteria, we approximated the local optima distribution by a reduced two-dimensional optimization problem. We reduced v_2, v_5 into one parameter, by setting $v_2 = v_5$, which is noted as v_0 . The other two parameter from the original problem are eliminated by fixing $v_1 = v_4 = 20$ nm. And the last parameter is v_3 , which is the distance between the two cylinders. Then the optimization problem reduces to a two-dimensional optimization problem with parameters v_0 and v_3 . With the OpenMaxwell as solver, we scan v_0 from 20 nm to 150 nm, and v_3 from 20 nm to 600 nm. Figure 4.8 shows the fitness function with respect to these two parameters. From the figure one can observe the distribution of the local optima for the reduced 2D optimization problem. From this information, one can approximate the distribution of the local optima for the original 5D problem. Our Nelder-Mead starting point is close to the global optimum, therefore the optimization result is the global one.

However, different choices of the starting point can lead to a globally non-optimal solution. It is very important to make a good initial guess for the Nelder-Mead method and other deterministic optimization methods. Unfortunately, most of the plasmonic optimizations are high dimensional, and it is hard to make good initial guesses. Therefore, even though the computational cost can be very high, it is recommended to use the ES optimization for plasmonic problems because of the higher probability to find the global optimum.

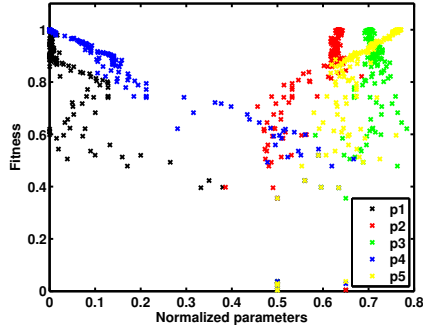


Figure 4.7: Five-dimensional optimization using Nelder-Mead method in COMSOL. There are 172 instances of simulations, with optimality tolerance of 0.01 and the initial values of the optimization set to be the mid-point of the corresponding parameter bounds. p_1 to p_5 are the normalized geometrical parameters, which are mentioned in section 4.3. The figure shows the distribution of the parameters versus the fitness function.

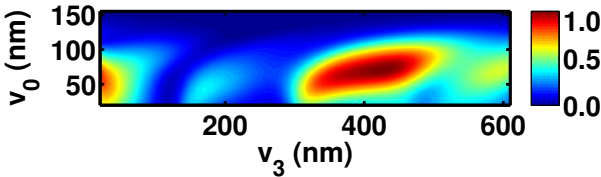


Figure 4.8: The fitness function of a two-dimensional scan using OpenMaXwell. The scanning parameters are the distance between the two cylinders v_3 , and the lower distance from the substrate v_0 , respectively.

4.6.2 The second test problem

We keep the same optimization configuration as in 4.6.1, *i. e.*, number of parents $\mu = 5$, number of children $\lambda = 35$, and mutation strength $\sigma = 0.1$. Figure 4.9 shows the convergence and the parameter distribution from a single optimization run. The optimization converges to the local optimum $\hat{F} = 0.54$ with $l = 109.2$ nm, $d = 592.0$ nm, and $h = 409.9$ nm, rather than to converge to the global optimum with $l = 114.9$ nm, $d = 268.4$ nm, and $h = 484.1$ nm.

To study the possible reasons of the failed convergence, we examine the

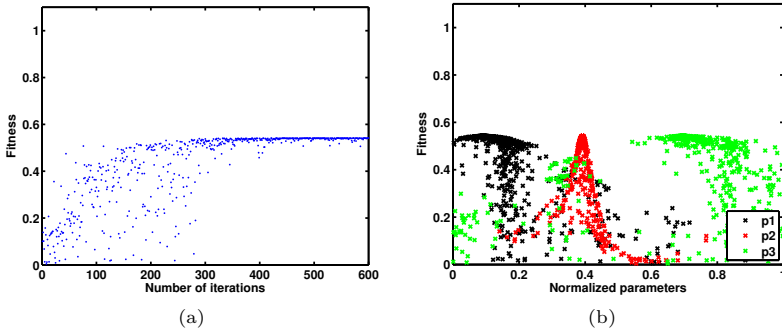


Figure 4.9: The results of the optimization with the strength of mutation $\sigma = 0.1$. The maximum number of individual simulations is 600, with the number of parents $\mu = 5$, number of children $\lambda = 35$. p_1 to p_3 are the normalized geometrical parameters, which are mentioned in section 4.3. The strategy keeps the best 5 parent individuals in each generation. (a) shows the convergence with respect to the number of iterations, and (b) shows the distribution of the normalized parameters versus the fitness function. The maximum fitness only reaches 0.54, since the optimization failed to find the global optimum.

smoothness of the fitness function. We perform several parameter scans near the global optimum. In each scan, two parameters are fixed to the global optimum values, and the third one is scanned in the range that covers the region of optimum. The results are shown in Figure 4.10.

In Figure 4.10a, h, d are fixed (484.1 nm and 268.4 nm respectively), and l is scanned from 100 to 200 nm. In Figure 4.10b, l, h are fixed (114.9 nm and 484.1 nm respectively), and d is scanned from 200 to 1200 nm. In Figure 4.10c, l, d are fixed (114.9 nm and 268.4 nm respectively), and h is scanned from 200 to 500 nm. From the scan plot, one can observe that \hat{F} is strongly sensitive to d near the global optimum. Therefore, the optimization with small $\sigma = 0.1$ has difficulties to catch the global optimum.

In order to search less focused, we increase σ to 0.2 and run the optimizations ten times for comparison. Figure 4.11 shows the convergence and the parameter distribution from the best optimization. The best fitness is reached with parameters $l = 114.9$ nm, $d = 268.4$ nm and $h = 484.1$ nm, which is the global optimum. The convergence is a bit slower than that in Figure 4.9, where a smaller σ is applied. From Figure 4.11b, one can observe that the distribution of the parameter p_2 is very narrow, therefore, it's very difficult to catch this

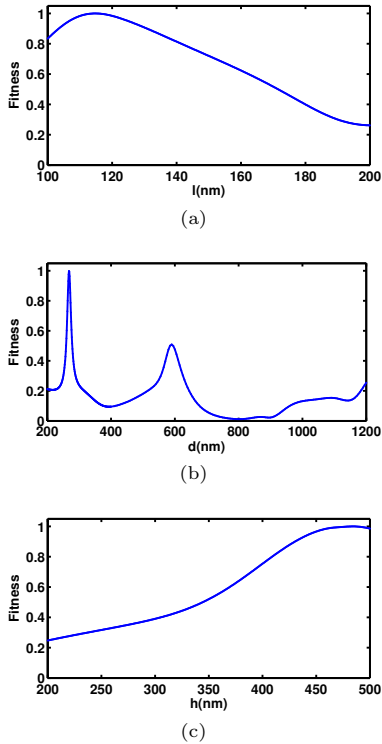


Figure 4.10: The results of the scan of the three optimization parameters. The scans are performed with the other two parameters set to the values of the global optimum. (a) shows the scan of l , (b) shows the scan of d , and (c) shows the scan of h . One can observe that the scan of d has a very sharp peak at the global optimum between 200 and 400 nm.

optimum when σ is small.

To conclude, a smaller mutation strength σ can lead to faster convergence, but may lead to possible failure in the search of global optimum. Based on the research above, an optimization strategy for general problems is proposed: Firstly, we select wide ranges of the optimization parameters and use big σ values. The convergence will be slow but the search figures out the approximated global optimum. Secondly, with the knowledge of the first step, we reduce the range of the optimization parameters around the optimum of the first step.

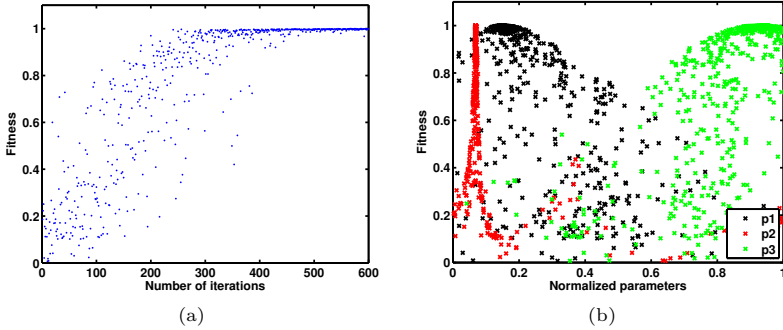


Figure 4.11: The results of the optimization with the variation parameter $\sigma = 0.2$. The maximum number of individual simulations is 600, the number of parents $\mu = 5$, and the number of children $\lambda = 35$. p_1 to p_3 are the normalized geometrical parameters, which are mentioned in section 4.3. The ES keeps the best 5 parent individuals in each generation. (a) shows the convergence with respect to the number of iterations, and (b) shows the distribution of the normalized parameters versus the fitness function. The maximum normalized fitness reaches 1.0, which corresponds to the global optimum.

Then we perform finer optimizations with smaller σ , in order to determine the global optimum more precisely. Finally, we check the smoothness near the global optimum found in the previous step, in order to check possible fabrication tolerances. Note that this step can be skipped if the distribution is smooth and exhibits no sharp peaks.

4.7 Summary

Two different, ultra short plasmon-assisted waveguide couplers were optimized using various methods. We have employed a robust optimizer based on an evolution strategy (ES), representing the category of nature-inspired optimization algorithms. **CONCEPTs** and the multiple multipole program (MMP) were used as different field solvers. **CONCEPTs** is a high-order FEM library. In order to link **CONCEPTs** with the optimizer and the mesh generator, a framework of parametric mesh generation was implemented. MMP is an element-free boundary discretization technique. For smooth geometry, it can provide very accurate solutions close to the analytic ones. We performed a statistical analysis of the optimizer, and showed that the results obtained with **CONCEPTs** and MMP

solvers converge to the same optimum. The optimizer is robust but due to randomness, the optimization convergence looked different each time, even with the same solver using exactly the same parameters.

For the first test problem, we also used the Nelder-Mead method, which is a deterministic optimization algorithm, that is contained in `COMSOL Multiphysics`. The Nelder-Mead method is very efficient but with the following requirements: the number of dimensions of the optimization should be low, and there are not many local optima within the search space. Our test problem is five-dimensional, which fulfills the first requirement. In order to check the second requirement, we scanned the reduced problem with only two parameters, and the approximated local optima distribution proved that Nelder-Mead can be applicable for our problem within the given range of the parameters. In order to find the global optimum, it must be started from point that are sufficiently close to the optimum.

Note that our first test problem only contains a pair of circular wires that may be described by 5 parameters. For increasing the coupling quality, more wires may be introduced. Each additional wire leads to 3 additional parameters. Thus, the dimension of the optimization problem becomes too high for Nelder Mead when a few wires are added. More importantly, it is very difficult to make a good initial guess in a high-dimensional search space. Without such a guess, it is likely that the deterministic optimizer sticks in a local optimum. Therefore, although the computational cost of performing an ES optimization can be very high, it is outweighed by its much higher probability to find the global optimum.

In the second test problem, we applied scatterers with sharp corners. Although we reduced the dimension of the optimization problem to only 3, the fitness changes rapidly in some regions. As a result, the ES optimizer may not catch the global optimum if the mutation strength σ is small. By increasing σ we found the global optimum. Based on this discovery, we proposed a general strategy to find the global optimum. Note that MMP would be inefficient for this problem because of sharp corners and triple points, which lead to field singularity and destroy the exponential convergence of MMP. Furthermore, Nelder Mead would not lead to the global optimum except when started in its close vicinity.

5 Conclusion

5.1 Summary

In this thesis, an accurate and efficient numerical solver has been implemented for plasmonics in layered media. The solver was implemented in the high order FEM package **CONCEPTs**. Several two-dimensional applications have been studied. Based on the solver, a framework for the optimization of plasmonic structures has been established. The optimizer applies ES and shows convergence towards the global optimum. The solver is combined with the parametric mesh generator of **COMSOL**. Several applications of plasmonics in layered media have been optimized.

This thesis starts with a discussion to select proper solvers. In chapter 2, the solvers were categorized by several criteria. In section 2.2, we have discussed that it is beneficial for plasmonics to employ FD, domain discretization solver with structured meshes. The boundary discretization solver MMP can be used as reference solution for benchmark problems with simple geometries. In section 2.3, we discussed that high order, curvilinear elements are beneficial. As a result, the high order, curvilinear FEM package **CONCEPTs** was selected.

In chapter 3, several truncation techniques have been studied and implemented in **CONCEPTs**. Truncation is an important issue in the FEM simulation of plasmonics, both in the free space scattering and the scattering in waveguides. In section 3.2, the ABC has been formulated and implemented for the free space scattering. The BGT conditions of 0th, 1st, and 2nd orders were implemented and compared. hp -analyses were performed. There is a limitation of the model by the domain size. The closer the boundary is placed, the more model error will increase. p -convergence is faster than h -convergence when the objects are smooth. On the other hand, the system matrix is sparse and the condition number is not high. As a comparison, the matrices in MMP are ill-conditioned, but with very small size. Therefore, MMP is excellent to provide reference solutions for smooth objects, while FEM is better in the simulation of more complicated geometries. In section 3.3, PML has been formulated and implemented for plasmonics in layered media. The PML shows good absorption even in the presence of strong guided waves. We studied the PML thoroughly by hp -analysis. Different schemes of h - and p -refinement are used inside the PML, and in the physical domains. The level of the p -refinement inside the physical domain dominates the saturation level of overall error. Inside the PML domain, the solution is exponentially decaying, therefore it is beneficial to apply

adaptive mesh refinement. Based on all these discoveries, an hp -strategy has been developed. It converges to high accuracy with a small additional cost of DOFs.

With our implementation of PML for layered media, we were able to establish the framework of optimization in chapter 4. The framework is a combination of an ES optimizer with the `CONCEPTs` solver, which is shown in figure 4.3. In order to realize parametric mesh generation, we linked `COMSOL` and `CONCEPTs` through a MATLAB script. The first test problem contains two cylindrical scatterers inside layered media. The scatterers compose an ultra-short plasmonic coupler. The design of the coupler leads to a five-dimensional optimization problem. In order to validate our results, we also used MMP as reference. A statistical analysis of the optimizers showed that the `CONCEPTs` and MMP results converge to the same optimum. Due to randomness in the search procedure, the convergence paths of the optimization were different each time. The second test problem contains sharp corner and triple points. This problem leads to long computation times for MMP. Thus, it has not been optimized with MMP. We found that the fitness function changed rapidly in some regions. Therefore, the ES optimizer with standard settings failed to converge to the global optimum sometimes. A tuning of the mutation strength σ was performed to find the global optimum.

5.2 Outlook

In the future, the following work would be helpful.

1. In order to simulate more realistic problems, a 3D implementation is needed. In this thesis, only 2D problems are addressed. We always assume that the objects are infinite along the third direction. However, in practice, the objects also have limitations in the third direction. Therefore, a 2D simulation is only an approximation of the realistic model. It should be noted that a 3D version of `CONCEPTs` is under development in K. Schmidt's group in Matheon, TU Berlin.

2. It would be helpful to develop a built-in mesh generator for `CONCEPTs`. For all the applications, we either make the mesh by hand, or link with external mesh generators. This limits the use of `CONCEPTs` through all the platforms. A built-in mesh generator, or even a graphical user interface would be very useful.

3. For the optimization, it would be helpful to apply parallel computing, since each individual is simulated separately. However, generation based optimizers limit the use of parallel computing. The reason is that in each generation, the optimizer needs to wait the slowest individual to finish. Therefore, generation-free optimizers would be more promising.

A Dielectric scattering formulation and implementation

Absorbing boundary conditions

The Sommerfeld radiation condition, as shown in A.1, characterizes outgoing scattered field u^{sc} .

$$\lim_{r \rightarrow \infty} r^{1/2} \left(\frac{\partial u^{\text{sc}}}{\partial r} - ik_0 u^{\text{sc}} \right) = 0 \quad (\text{A.1})$$

However, since it approaches infinity, the Sommerfeld condition can not be implemented numerically. Therefore, we need to replace the Sommerfeld condition with a boundary condition on a truncated domain with radius R , as shown in figure A.1. Denote Γ_0 the boundary of the truncated computation domain. The

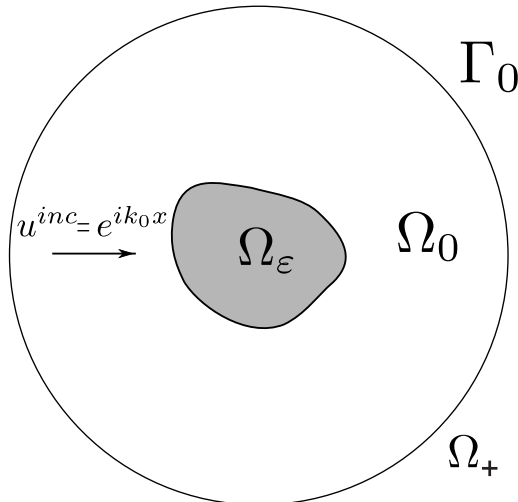


Figure A.1: The computation domain of dielectric scattering problem.

absorbing boundary condition have the following form.

$$\frac{\partial u^{\text{sc}}}{\partial r} + \alpha u^{\text{sc}} + \beta \frac{\partial^2 u^{\text{sc}}}{\partial \theta^2} = 0, \quad \vec{x} \in \Gamma_0 \quad (\text{A.2})$$

This is called Bayliss-Gunzburger-Turkel (BGT) conditions, which are a sequence of boundary operators based on an asymptotic expansion in $k_0 R$. The 0th to 2nd BGT boundary conditions are shown in table(A.1)

Type	α	β
BGT-0	$-ik_0$	0
BGT-1	$-ik_0 + \frac{1}{2R}$	0
BGT-2	$-ik_0 + \frac{1}{2R} - \frac{1}{8R(1-ik_0R)}$	$-\frac{1}{2R(1-ik_0R)}$

Table A.1: The coefficients of BGT absorbing boundary conditions

TM case

We define Ω the computational domain, which consists of two parts: Ω_ϵ and Ω_0 , where Ω_ϵ is the space with spatial dependent dielectric material $\epsilon(\vec{x})$, and Ω_0 is the free space. $\Omega = \Omega_\epsilon \cup \Omega_0$. In order to derive the boundary conditions, we denote Ω_+ the domain outside our computational domain. Γ_0 is the outer boundary of Ω , and is also the interface between Ω and Ω_+ . The geometry is shown in figure A.1.

We model the total electric field u . With BGT condition on Γ_0 , the field can

be truncated in Ω . For TM case the total field fulfill the following equations.

$$\begin{aligned} -\Delta u - \epsilon(\vec{x})k_0^2 u &= 0 \quad \vec{x} \in \Omega \\ \frac{\partial u^{\text{sc}}}{\partial r} + \alpha u^{\text{sc}} + \beta \frac{\partial^2 u^{\text{sc}}}{\partial \theta^2} &= 0, \quad \vec{x} \in \Gamma_0 \end{aligned} \quad (\text{A.3})$$

Multiplying (A.3) by a test function v , integrating over Ω and then integrating by part, we obtain the variational formulation,

$$\text{find } u \in H^1(\Omega), \text{ s. t. } \Phi(u, v) = 0, \text{ for all } v \in H^1(\Omega), \quad (\text{A.4})$$

where

$$\Phi(u, v) = \int_{\Omega} (\nabla u \cdot \nabla v - \epsilon(\vec{x})k_0^2 uv) \, d\vec{x} - \int_{\Gamma_0} \partial_n uv \, ds.$$

The following shows how to formulate the edge integral $\int_{\Gamma_0} \partial_n uv \, ds$.

BGT-0 condition

u is the total electric field, and it is the global solution in $\Omega \cup \Omega_+$. Denote u_+ and u_- the solutions in Ω_+ and Ω , which fulfill

$$\begin{aligned} u_+ &= u \text{ in } \Omega_+ \\ u_+ &= 0 \text{ in } \Omega \\ u_- &= u \text{ in } \Omega \\ u_- &= 0 \text{ in } \Omega_+. \end{aligned}$$

In Ω_+ , $u_+ = u^{\text{sc}} + u^{\text{inc}}$, where u^{sc} is the scattered field and it is outgoing. Therefore, it fulfills BGT-0 condition, *i. e.*, $\partial_n u_+^{\text{sc}} = ik_0 u_+^{\text{sc}}$. In Ω , we have $u_- = u$. On Γ_0 , we have the continuity condition of $\partial_n u$ and u , *i. e.*, $\partial_n u_+ = \partial_n u_-$ and $u_+ = u_-$.

Summing up all together, we have the following equation on Γ_0 ,

$$\begin{aligned} \partial_n u_+^{\text{sc}} = \partial_n u_+ - \partial_n u^{\text{inc}} &= \partial_n u_- - \partial_n u^{\text{inc}} \\ \parallel & \\ ik_0 u_+^{\text{sc}} = ik_0(u_+ - u^{\text{inc}}) &= ik_0(u_- - u^{\text{inc}}) \end{aligned} \quad (\text{A.5})$$

which leads to,

$$\partial_n u = ik_0 u + \partial_n u^{\text{inc}} - ik_0 u^{\text{inc}} \quad (\text{A.6})$$

Plug (A.6) into (A.4), we get,

$$\int_{\Omega} (\nabla u \cdot \nabla v - \epsilon(\vec{x})k_0^2 uv) \, d\vec{x} - ik_0 \int_{\Gamma_0} uv \, ds = \int_{\Gamma_0} (\partial_n u^{\text{inc}} - ik_0 u^{\text{inc}}) v \, ds \quad (\text{A.7})$$

and this is the final formulation of dielectric scattering problem with BGT-0 absorbing boundary condition.

BGT-1 and BGT-2 conditions

For BGT-1 and BGT-2 conditions, similarly as BGT-0 condition, we apply the continuity condition on Γ_0 ,

$$\begin{aligned} \partial_n u_+^{\text{sc}} &= \partial_n u_+ - \partial_n u^{\text{inc}} = \partial_n u_- - \partial_n u^{\text{inc}} \\ \parallel \\ -\alpha u_+^{\text{sc}} - \beta \frac{\partial^2 u_+^{\text{sc}}}{\partial \theta^2} &= -\alpha(u_+ - u^{\text{inc}}) - \beta \frac{\partial^2 (u_+ - u^{\text{inc}})}{\partial \theta^2} \\ &= (-\alpha u_- - \beta \frac{\partial^2 u_-}{\partial \theta^2}) + (\alpha u^{\text{inc}} + \beta \frac{\partial^2 u^{\text{inc}}}{\partial \theta^2}) \end{aligned} \quad (\text{A.8})$$

Then we have,

$$\partial_n u = (-\alpha u - \beta \frac{\partial^2 u}{\partial \theta^2}) + (\alpha u^{\text{inc}} + \partial_n u^{\text{inc}} + \beta \frac{\partial^2 u^{\text{inc}}}{\partial \theta^2}) \quad (\text{A.9})$$

in order to plug (A.9) into (A.4), $-\int_{\Gamma_0} \partial_n uv \, ds$ needs to be computed separately,

$$-\int_{\Gamma_0} \partial_n uv \, ds = \int_{\Gamma_0} (\alpha u + \beta \frac{\partial^2 u}{\partial \theta^2}) v \, ds - \int_{\Gamma_0} (\alpha u^{\text{inc}} + \partial_n u^{\text{inc}} + \beta \frac{\partial^2 u^{\text{inc}}}{\partial \theta^2}) v \, ds \quad (\text{A.10})$$

integrate $\int_{\Gamma_0} \frac{\partial^2 u}{\partial \theta^2} v \, ds$ by parts, considering Γ_0 is an closed curve, the integral becomes

$$\int_{\Gamma_0} \frac{\partial^2 u}{\partial \theta^2} v \, ds = - \int_{\Gamma_0} \frac{\partial u}{\partial \theta} \frac{\partial v}{\partial \theta} \, ds + 0 \quad (\text{A.11})$$

Plug (A.10) into (A.4), then we get the final formulation,

$$\int_{\Omega} (\nabla u \cdot \nabla v - \epsilon(\vec{x}) k_0^2 uv) \, d\vec{x} + \int_{\Gamma_0} (\alpha uv - \beta \frac{\partial u}{\partial \theta} \frac{\partial v}{\partial \theta}) \, ds = \int_{\Gamma_0} (\alpha u^{\text{inc}} + \partial_n u^{\text{inc}} + \beta \frac{\partial^2 u^{\text{inc}}}{\partial \theta^2}) v \, ds \quad (\text{A.12})$$

TE case

TE case corresponds to the magnetic field in scattering problem.

$$-\nabla \cdot \left(\frac{1}{\epsilon(\vec{x})} \nabla u \right) - k_0^2 u = 0 \quad (\text{A.13})$$

integrate (A.13) with test function v then integrate by parts, one obtains,

$$\begin{aligned} - \int_{\Omega} \nabla \cdot \left(\frac{1}{\epsilon(\vec{x})} \nabla u \right) v \, d\vec{x} &= \int_{\Omega} \frac{1}{\epsilon(\vec{x})} \nabla u \cdot \nabla v \, d\vec{x} - \int_{\Gamma_0} \frac{1}{\epsilon(\vec{x})} \partial_n uv \, ds \\ \Rightarrow \int_{\Omega} \frac{1}{\epsilon(\vec{x})} \nabla u \cdot \nabla v \, d\vec{x} - k_0^2 \int_{\Omega} uv \, d\vec{x} - \int_{\Gamma_0} \frac{1}{\epsilon(\vec{x})} \partial_n uv \, ds &= 0 \end{aligned} \quad (\text{A.14})$$

similarly as TM case, we have relationship (A.10). For TE scattering problem, $\epsilon(\vec{x})|_{\vec{x} \in \Gamma_0} = 1$, which makes the problem easier. Finally, we get formulation for TE scattering

$$\int_{\Omega} \left(\frac{1}{\epsilon(\vec{x})} \nabla u \cdot \nabla v - k_0^2 uv \right) d\vec{x} + \int_{\Gamma_0} (\alpha uv - \beta \frac{\partial u}{\partial \theta} \frac{\partial v}{\partial \theta}) ds = \int_{\Gamma_0} (\alpha u^{\text{inc}} + \partial_n u^{\text{inc}} + \beta \frac{\partial^2 u^{\text{inc}}}{\partial \theta^2}) v ds. \quad (\text{A.15})$$

Implementation in CONCEPTs

All the integral in the formulation can be implemented in CONCEPTs, the corresponding relationship are shown in table(A.2). In TM case, from (A.12), we

integral	CONCEPTs class	bilinear or linear	matrix	type
$\int_{\Omega} \nabla u \cdot \nabla v d\vec{x}$	hp2D::Laplace	bilinear	\mathcal{S}	element stiffness matrix
$\int_{\Omega} uv d\vec{x}$	hp2D::Identity	bilinear	\mathcal{M}	element mass matrix
$\int_{\Gamma_0} \frac{\partial u}{\partial s} \frac{\partial v}{\partial s} ds$	hp1D::Laplace	bilinear	\mathcal{S}_e	edge stiffness matrix
$\int_{\Gamma_0} uv ds$	hp1D::Identity	bilinear	\mathcal{M}_e	edge mass matrix
$\int_{\Gamma_0} f v ds$	hp1D::Riesz	linear	$rhs(\text{vector})$	load vector

Table A.2: The implementation of the integral in CONCEPTs

solve the system

$$(\mathcal{S} - k_0^2 \mathcal{M}(\epsilon) + \alpha \mathcal{S}_e - \beta \mathcal{M}_e)u = rhs \quad (\text{A.16})$$

In TE case, from (A.15), we solve the system

$$(\mathcal{S}(\epsilon) - k_0^2 \mathcal{M} + \alpha \mathcal{S}_e - \beta \mathcal{M}_e)u = rhs \quad (\text{A.17})$$

To construct matrix with piecewise constant epsilon, e.g. $\mathcal{S}(\epsilon)$, we need CONCEPTs class `concepts::PiecewiseConstFormula` to construct bilinear form from the integral $\int_{\Omega} \frac{1}{\epsilon(\vec{x})} \nabla u \cdot \nabla v d\vec{x}$. The following piece of code can construct $\mathcal{S}(\epsilon)$.

```
concepts::PiecewiseConstFormula<Cmplx> epsilon;
hp2D::Laplace<Cmplx> la(epsilon);
concepts::SparseMatrix<Cmplx> stiff(space, la);
```


Bibliography

- [1] P. Bharadwaj, B. Deutsch, and L. Novotny, “Optical antennas,” *Advances in Optics and Photonics*, Vol. 1, No. 3, pp. 438–483, 2009.
- [2] L. Novotny and B. Hecht, *Principles of nano-optics*. Cambridge university press, 2012.
- [3] J. Smajic, C. Hafner, and D. Erni, “Design and optimization of an achromatic photonic crystal bend,” *Opt. Express*, Vol. 11, No. 12, pp. 1378–1384, 2003.
- [4] M. E. Stewart, C. R. Anderton, L. B. Thompson, J. Maria, S. K. Gray, J. A. Rogers, and R. G. Nuzzo, “Nanostructured plasmonic sensors,” *Chemical reviews*, Vol. 108, No. 2, pp. 494–521, 2008.
- [5] T. Sannomiya, C. Hafner, and J. Voros, “In situ sensing of single binding events by localized surface plasmon resonance,” *Nano letters*, Vol. 8, No. 10, pp. 3450–3455, 2008.
- [6] T. Sannomiya, C. Hafner, and J. Vörös, “Plasmonic nanoparticle based biosensing: experiments and simulations,” in *SPIE NanoScience+ Engineering*. International Society for Optics and Photonics, 2009, pp. 73 950M–73 950M.
- [7] M. Wang, C. Engstrom, K. Schmidt, and C. Hafner, “On high-order fem applied to canonical scattering problems in plasmonics,” *Journal of Computational and Theoretical Nanoscience*, Vol. 8, No. 8, pp. 1564–1572, 2011.
- [8] M. Wang, K. Schmidt, A. Alparslan, and C. V. Hafner, “Hp-fem and pml analysis of plasmonic particles in layered media,” *Progress In Electromagnetics Research*, Vol. 142, pp. 523–544, 2013.
- [9] M. Wang, A. Alparslan, S. M. Schnepf, and C. Hafner, “Optimization of a plasmon-assisted waveguide coupler using fem and mmp,” *Progress In Electromagnetics Research B*, Vol. 59, pp. 219–229, 2014.
- [10] Y. Fang, N. Seong, and D. Dlott, “Measurement of the distribution of site enhancements in surface-enhanced Raman scattering,” *Science*, Vol. 321, No. 5887, p. 388, 2008.

-
- [11] A. Taflove, *Computational electrodynamics: The Finite-Difference Time-Domain Method*. Boston, London: Artech House, 1995.
- [12] J. Jin, *The Finite Element Method in Electromagnetics*. New York: John Wiley & Sons, 1993.
- [13] P. Frauenfelder and C. Lage, “Concepts—an object-oriented software package for partial differential equations,” *Math Model Numer Anal.*, Vol. 36, No. 5, pp. 937–951, 2002.
- [14] K. Schmidt, “High-order numerical modeling of highly conductive thin sheets,” Ph.D. dissertation, ETH Zurich, July 2008.
- [15] K. Schmidt and P. Kauf, “Computation of the band structure of two-dimensional photonic crystals with *hp* finite elements,” *Comput. Methods Appl. Mech. Engrg.*, Vol. 198, pp. 1249–1259, 2009.
- [16] K. Schmidt and R. Kappeler, “Efficient computation of photonic crystal waveguide modes with dispersive material,” *Optics Express*, Vol. 18, No. 7, pp. 7307–7322, 2010.
- [17] C. Hafner, *MaX-1: a visual electromagnetics platform for PCs*. John Wiley & Sons Chichester, UK, 1999.
- [18] C. Hafner, *Post-modern electromagnetics: using intelligent Maxwell solvers*. Wiley, 1999.
- [19] A. Alparslan and C. Hafner, “Using Layered Geometry Green’s Functions in the Multiple Multipole Program,” *Journal of Computational and Theoretical Nanoscience*, Vol. 8, No. 8, pp. 1600–1608, 2011.
- [20] A. Alparslan and C. Hafner, “Analysis of Photonic Structures by the Multiple Multipole Program with Complex Origin Layered Geometry Green’s Functions,” *Journal of Computational and Theoretical Nanoscience*, Vol. 9, No. 3, pp. 479–485, 2012.
- [21] A. Alparslan, “Numerical analysis of photonic nanostructures in layered geometries,” Ph.D. dissertation, ETH Zurich, Switzerland, 2013.
- [22] S. M. Rao, *Time domain electromagnetics*. Academic Press, 1999.
- [23] K. S. Yee, “Numerical solution of initial boundary value problems involving Maxwell’s equations in isotropic media,” *IEEE Trans. Antennas Propagat.*, Vol. 14, pp. 302–307, May 1966.

- [24] J. S. Hesthaven and T. Warburton, *Nodal Discontinuous Galerkin Methods*. Berlin: Springer-Verlag, 2008.
- [25] R. J. LeVeque, *Finite volume methods for hyperbolic problems*. Cambridge university press, 2002, Vol. 31.
- [26] J. Crank *et al.*, “The mathematics of diffusion,” 1975.
- [27] J. D. Jackson, *Classical Electrodynamics*, 3rd Ed. New York: John Wiley & Sons, 1999.
- [28] C. Hafner, “Drude model replacement by symbolic regression,” *Journal of Computational and Theoretical Nanoscience*, Vol. 2, No. 1, pp. 88–98, 2005.
- [29] E. D. Palik, *Handbook of Optical Constants of Solids*. New York: Academic Press, 1985.
- [30] P. B. Johnson and R. W. Christy, “Optical constants of the noble metals,” *Phys. Rev. B*, Vol. 6, No. 12, pp. 4370–4379, 1972.
- [31] R. F. Harrington, *Field Computation by Moment Methods*. New York: Macmillan, 1968.
- [32] T. Kaufmann, C. Fumeaux, and R. Vahldieck, “The meshless radial point interpolation method for time-domain electromagnetics,” in *Microwave Symposium Digest, 2008 IEEE MTT-S International*. IEEE, 2008, pp. 61–64.
- [33] G. Mie, “Beiträge zur optik trüber medien, speziell kolloidaler metallösungen,” *Annalen der physik*, Vol. 330, No. 3, pp. 377–445, 1908.
- [34] A. C. Cangellaris and D. B. Wright, “Analysis of the numerical error caused by the stair-stepped approximation of a conducting boundary in fddt simulations of electromagnetic phenomena,” *Antennas and Propagation, IEEE Transactions on*, Vol. 39, No. 10, pp. 1518–1525, 1991.
- [35] M. Okoniewski, E. Okoniewska, and M. A. Stuchly, “Three-dimensional subgridding algorithm for fddt,” *Antennas and Propagation, IEEE Transactions on*, Vol. 45, No. 3, pp. 422–429, 1997.
- [36] “COMSOL Multiphysics,” <http://www.comsol.com/>.
- [37] “EZ4U. Mesh generation environment,” www.lacan.upc.edu/ez4u.htm.
- [38] L. Demkowicz, *Computing with hp-adaptive finite elements: One and Two Dimensional Elliptic and Maxwell problems*. Chapman and Hall / CRC Applied Mathematics and Nonlinear Science, 2006.

- [39] G. E. Karniadakis and S. J. Sherwin, *Spectral/hp Element Methods for Computational Fluid Dynamics*. Oxford: Oxford University Press, 2005.
- [40] C. Schwab, *p- and hp- Finite Element Methods: Theory and Applications in Solid and Fluid Mechanics*. Oxford University Press, 1998.
- [41] J. Shirron and I. Babuška, “A comparison of approximate boundary conditions and infinite element methods for exterior Helmholtz problems,” *Computer Methods in Applied Mechanics and Engineering*, Vol. 164, No. 1-2, pp. 121–139, 1998.
- [42] C. Engström, “On a high-order discontinuous galerkin method applied to canonical scattering problems,” in *International Symposium on Electromagnetic Theory (EMTS 2010), Berlin, Germany*, August 16– 19 2010, pp. 907–910.
- [43] L. Demkowicz, *Computing with Hp-adaptive Finite Elements: One and two dimensional elliptic and Maxwell problems*. CRC Press, 2006.
- [44] A. Sommerfeld, *Partial differential equations in physics*. New York: Academic Press, 1949.
- [45] A. Bayliss, M. Gunzburger, and E. Turkel, “Boundary conditions for the numerical solution of elliptic equations in exterior domains,” *SIAM J. Appl. Math.*, Vol. 42, No. 2, pp. 430–451, 1982.
- [46] F. Ihlenburg, *Finite element analysis of acoustic scattering*. Berlin: Springer-Verlag, 1998.
- [47] C. Lee, R. Shin, J. Kong, and B. McCartin, “Absorbing boundary conditions on circular and elliptical boundaries,” *Journal of Electromagnetic Waves and Applications*, Vol. 4, No. 10, pp. 945–962, 1990.
- [48] H. Barucq, R. Djellouli, and A. Saint-Guirons, “Performance assessment of a new class of local absorbing boundary conditions for elliptical- and prolate spheroidal-shaped boundaries,” *Applied Numerical Mathematics*, Vol. 59, No. 7, pp. 1467–1498, 2009.
- [49] P. Frauenfelder, “hp-finite element methods on anisotropically, locally refined meshes in three dimensions with stochastic data,” PhD thesis, ETH Zrich, Zrich, 2004. [Online]. Available: <http://e-collection.ethbib.ethz.ch/view/eth:27514>
- [50] M. Ainsworth and J. Coyle, “Conditioning of hierarchic p-version Nédélec elements on meshes of curvilinear quadrilaterals and hexahedra,” *SIAM Journal on Numerical Analysis*, Vol. 41, No. 2, pp. 731–750, 2004.

- [51] J. W. Demmel, S. C. Eisenstat, J. R. Gilbert, X. S. Li, and J. W. H. Liu, “A supernodal approach to sparse partial pivoting,” *SIAM J. Matrix Analysis and Applications*, Vol. 20, No. 3, pp. 720–755, 1999.
- [52] J. Smajic, C. Hafner, L. Raguin, K. Tavzarashvili, and M. Mishrikey, “Comparison of numerical methods for the analysis of plasmonic structures,” *J. Comput. Theor. Nanosci.*, Vol. 6, pp. 1–12, 2009.
- [53] M. Ainsworth, “Discrete dispersion relation for hp-version finite element approximation at high wave number,” *SIAM Journal on Numerical Analysis*, Vol. 42, No. 2, pp. 553–575, 2005.
- [54] T. Hagstrom, T. Warburton, and D. Givoli, “Radiation boundary conditions for time-dependent waves based on complete plane wave expansions,” *Journal of Computational and Applied Mathematics*, 2009.
- [55] C. Engström, C. Hafner, and K. Schmidt, “Comutations of lossy bloch waves in two-dimensional photonic crystals,” *J. Comput. Theor. Nanosci.*, Vol. 6, pp. 775–783, 2009.
- [56] J. A. Kong, *Electromagnetic wave theory*. Wiley New York et al., 1986.
- [57] F. Ihlenburg, *Finite Element Analysis of Acoustic Scattering*. Berlin & Heidelberg, Germany: Springer, 1998.
- [58] D. Givoli, *Numerical methods for problems in infinite domains*. Amsterdam and New York: Elsevier, 1992.
- [59] A.-S. Bonnet-BenDhia, G. Dakhia, C. Hazard, and L. Chorfi, “Diffraction by a defect in an open waveguide : a mathematical analysis based on a modal radiation condition.” *SIAM J. Appl. Math.*, Vol. 70, No. 3, pp. 677–693, 7 2009.
- [60] G. Ciruolo and R. Magnanini, “A radiation condition for uniqueness in a wave propagation problem for 2-d open waveguides,” *Math. Meth. Appl. Sci.*, Vol. 32, No. 10, pp. 1183–1206, 2009.
- [61] A.-S. Bonnet-BenDhia, B. Goursaud, and C. Hazard, “Mathematical analysis of the junction of two acoustic open waveguides,” *SIAM J. Appl. Math.*, Vol. 71, pp. 2048–2071, 2011.
- [62] C. Jerez-Hanckes and J.-C. Nédélec, “Asymptotics for helmoltz and maxwell solutions in 3-d open waveguides,” *Commun. Comput. Phys.*, Vol. 11, No. 2, pp. 629–646, Feb 2012.

-
- [63] F. Schmidt, "A new approach to coupled interior-exterior helmholtz-type problems: Theory and algorithms," Habilitation thesis, Free University Berlin, Germany, 2002.
- [64] M. Aksun and G. Dural, "Clarification of issues on the closed-form green's functions in stratified media," *Antennas and Propagation, IEEE Transactions on*, Vol. 53, No. 11, pp. 3644–3653, 2005.
- [65] A. Alparslan, M. Aksun, and K. A. Michalski, "Closed-form Green's functions in planar layered media for all ranges and materials," *Microwave Theory and Techniques, IEEE Transactions on*, Vol. 58, No. 3, pp. 602–613, 2010.
- [66] J.-P. Berenger, "A perfectly matched layer for the absorption of electromagnetic waves," *Journal of computational physics*, Vol. 114, No. 2, pp. 185–200, 1994.
- [67] J.-M. Jin and W. C. Chew, "Combining PML and ABC for the finite-element analysis of scattering problems," *Microwave and Optical Technology Letters*, Vol. 12, No. 4, pp. 192–197, 1996.
- [68] W. C. Chew, W. H. Weedon, and A. Sezginer, "A 3-D perfectly matched medium by coordinate stretching and its absorption of static fields," in *Applied Computational Electromagnetics Symposium Digest*, Vol. 1. Citeseer, 1995, pp. 482–489.
- [69] A. Bermúdez, L. Hervella-Nieto, and A. Prieto, "An optimal perfectly matched layer with unbounded absorbing function for time-harmonic acoustic scattering problems," *Journal of Computational Physics*, Vol. 223, No. 2, pp. 469–488, 2007.
- [70] F. Collino and P. Monk, "The perfectly matched layer in curvilinear coordinates," *SIAM Journal on Scientific Computing*, Vol. 19, No. 6, pp. 2061–2090, 1998.
- [71] L. Zschiedrich, R. Klose, A. Schädle, and F. Schmidt, "A new finite element realization of the perfectly matched layer method for helmholtz scattering problems on polygonal domains in two dimensions," *Journal of Computational and Applied Mathematics*, Vol. 188, No. 1, pp. 12–32, 2006.
- [72] Z. Chen and H. Wu, "An adaptive finite element method with perfectly matched absorbing layers for the wave scattering by periodic structures," *SIAM J. Numer. Anal.*, Vol. 41, No. 3, pp. 799–826, 2003.

- [73] G. Bao, Z. Chen, and H. Wu, “Adaptive finite-element method for diffraction gratings,” *JOSA A*, Vol. 22, No. 6, pp. 1106–1114, 2005.
- [74] C. Michler, L. Demkowicz, J. Kurtz, and D. Pardo, “Improving the performance of perfectly matched layers by means of hp-adaptivity,” *Numerical Methods for Partial Differential Equations*, Vol. 23, No. 4, pp. 832–858, 2007. [Online]. Available: <http://dx.doi.org/10.1002/num.20252>
- [75] L. Zschiedrich, “Transparent boundary conditions for maxwell’s equations,” Ph.D. dissertation, FU Berlin, Berlin, Germany, Nov 2009.
- [76] L. Nannen and A. Schädle, “Hardy space infinite elements for helmholtz-type problems with unbounded inhomogeneities,” *Wave Motion*, Vol. 48, No. 2, pp. 116–129, 2011.
- [77] B. Kettner and F. Schmidt, “The pole condition as transparent boundary condition for resonance problems: detection of spurious modes,” 2011, pp. 79 331B–79 331B–11. [Online]. Available: <http://dx.doi.org/10.1117/12.874752>
- [78] B. Kettner, “Detection of spurious modes in resonance mode computations – pole condition method,” PhD thesis, FU Berlin, Berlin, Germany, July 2012.
- [79] K. Schmidt and P. Kauf, “Computation of the band structure of two-dimensional photonic crystals with *hp* finite elements,” *Comp. Meth. App. Mech. Engr.*, Vol. 198, pp. 1249–1259, March 2009.
- [80] J. Sarrate Ramos and A. Huerta, “Efficient unstructured quadrilateral mesh generation,” *International Journal for Numerical Methods in Engineering*, Vol. 49, pp. 1327–1350, 2010.
- [81] J. M. Melenk and S. Sauter, “Convergence analysis for finite element discretizations of the Helmholtz equation with Dirichlet-to-Neumann boundary conditions,” *Math. Comp.*, Vol. 79, No. 272, pp. 1871–1914, 2010.
- [82] J. M. Melenk and S. Sauter, “Wavenumber explicit convergence analysis for galerkin discretizations of the helmholtz equation,” *SIAM Journal on Numerical Analysis*, Vol. 49, No. 3, pp. 1210–1243, 2011.
- [83] J. N. Anker, W. P. Hall, O. Lyandres, N. C. Shah, J. Zhao, and R. P. Van Duyne, “Biosensing with plasmonic nanosensors,” *Nature materials*, Vol. 7, No. 6, pp. 442–453, 2008.

- [84] A. Baron, E. Devaux, J.-C. Rodier, J.-P. Hugonin, E. Rousseau, C. Genet, T. W. Ebbesen, and P. Lalanne, “Compact antenna for efficient and unidirectional launching and decoupling of surface plasmons,” *Nano letters*, Vol. 11, No. 10, pp. 4207–4212, 2011.
- [85] M. Esslinger, W. Khunsin, N. Talebi, T. Wei, J. Dorfmüller, R. Vogelgesang, and K. Kern, “Phase engineering of subwavelength unidirectional plasmon launchers,” *Advanced Optical Materials*, Vol. 1, No. 6, pp. 434–437, 2013.
- [86] C. A. Balanis, *Antenna theory: analysis and design*. John Wiley & Sons, 2012.
- [87] N. Komarevskiy, V. Shklover, L. Braginsky, C. Hafner, and J. Lawson, “Potential of glassy carbon and silicon carbide photonic structures as electromagnetic radiation shields for atmospheric re-entry,” *Optics express*, Vol. 20, No. 13, pp. 14 189–14 200, 2012.
- [88] M. Esslinger, “Nearfield optical interactions of nano-plasmonic particle assemblies,” Ph.D. dissertation, ÉCOLE POLYTECHNIQUE FÉDÉRALE DE LAUSANNE, 2013.
- [89] J.-F. Bonnans, J. C. Gilbert, C. Lemaréchal, and C. A. Sagastizábal, *Numerical optimization: theoretical and practical aspects*. Springer, 2006.
- [90] J. A. Nelder and R. Mead, “A simplex method for function minimization,” *Computer journal*, Vol. 7, No. 4, pp. 308–313, 1965.
- [91] J. Brownlee, *Clever Algorithms: Nature-Inspired Programming Recipes*. Jason Brownlee, 2011.
- [92] J. M. Johnson and V. Rahmat-Samii, “Genetic algorithms in engineering electromagnetics,” *Antennas and Propagation Magazine, IEEE*, Vol. 39, No. 4, pp. 7–21, 1997.
- [93] H.-G. Beyer and H.-P. Schwefel, “Evolution strategies—a comprehensive introduction,” *Natural computing*, Vol. 1, No. 1, pp. 3–52, 2002.
- [94] “Ch. Hafner’s Generalized Genetic Program (GGP),” <http://alphard.ethz.ch/Hafner/ggp/gp.htm>.
- [95] A. Taflov and S. C. Hagness, *Computational electrodynamics*. Artech house Boston, 2000, Vol. 160.
- [96] A. Bayliss, M. Gunzburger, and E. Turkel, “Boundary conditions for the numerical solution of elliptic equations in exterior regions,” *SIAM Journal on Applied Mathematics*, Vol. 42, No. 2, pp. 430–451, 1982.

[97] “OpenMaXwell,” <http://openmax.ethz.ch/>.

Acknowledgments

This thesis was carried out at the Institute of Electromagnetic Fields (IEF, formerly IFH) of the Swiss Federal Institute of Technology Zurich (*Eidgenössische Technische Hochschule Zürich*, ETH). The work was funded by the Swiss National Science Foundation (SNSF200021-119813) and the internal fund of the institute.

First of all, I would really appreciate my supervisor Prof. Christian Hafner. He gave me great guidance and support in my research and life. He has great knowledge of numerical simulations and optimizations, and led the way of my PhD. He has great insight of science, and he is also an artist in painting and music. He thinks that MMP is among his best art work. He constantly supported my research, and he even review my publications line by line. He offered great help when I faced trouble. Without his support, I would never finish the degree. He will retire quite soon, I wish him all the best. I would thank Prof. Ralf Hiptmair who accepted to be the co-examiner. He was also my recommender to open the chance of my PhD study in ETH. His great knowledge of numerical methods helps me a lot in the numerical analysis. I would thank Prof. Jürg Leuthold who took charge of the institute in the last year of my PhD. He continued to support the former PhD students. I would also memorize Prof. Rüdiger Vahldieck, who passed away due to tragic illness. I still remember the afternoon in Singapore he interviewed and chatted with me for the first time.

My special acknowledgement to my direct supervisors, Dr. Christian Engström and Dr. Kersten Schmidt. Dr. Christian Engström was my direct supervisor for the first half of my PhD. He taught me how to conduct research and helped me in details from coding to scientific writing, and he broadened my perspective of finite element methods. He is also my friend in real life, he has great personality that everyone in the institute liked him. I enjoyed many talks with him in various topics from politics to science fantasies. He established family with his wife Annette, and now their happy family are living with two children in Sweden. He continued his academic career in Umeå University in Sweden. I wish both his career and family all the best of luck in the future. Dr. Kersten Schmidt was my direct supervisor for the second half of my PhD. He gave me the greatest support and help in my project. He is a talented mathematician and programmer, and I learned so much from him. Now he is the authority of **CONCEPTs** and he established his group in TU Berlin. He invited me many times to his institute in Paris and Berlin. During our collaboration in Berlin, we implemented absorbing boundary conditions and perfectly matched

layers for layered geometries, which are the core part of my thesis. His team is continuing the development of **CONCEPTs** and making contributions. I wish him great career and all the best to his family. I also acknowledge Dr. Sascha Schnepf. In the last year of my PhD, he partly supervised me with his knowledge of numerical methods and contributed to my publication.

Furthermore, I would like to thank my co-workers in the/ project. Holger Brandsmeier in mathematics department helped me for coding of PML. I learned a lot of programming skills from him. My colleague Aytac Alparslan helped me in the concepts of layered geometries, and he also performed MMP validation for my FEM results. Nikolay Komarevsky shared his knowledge of optimization. Mustafa Boyvat helped me with **COMSOL** issues. I also thank my colleagues in TU-Berlin: Dirk, Robert, and Christian. I acknowledge our IT support Aldo Rossi and Dr. Pascal Leuchtman. And my thanks to our secretaries Barbara, Eva and Bettina.

Throughout my PhD I was so lucky to know so many nice colleagues. They are not only my colleagues but friends. I appreciate our "Barbecue team" that we had so much fun together: Dimitra and her husband Peggy, Aytac, Bora, Jan, Sam, and Nikolay. We enjoy so many barbecues and beers together, and the chats of all aspects: life, culture, politics, history, and fun. Even now we are going all around the world, I always feel we are together. I thank my colleagues Dirk, Thomas, Chris, Mustafa, Alex, Ping, Sahar, Pegah, Yannick, and Nemat for the great atmosphere during my PhD.

I would also thank my friends: Xia, Denis, Han, Yu, Xu, Judy, Ye, Christian, etc. for the valuable friendship and great fun in Switzerland. My final thanks give to my parents, who support me with endless love. Your love is my ultimate motivation to move forward. Even though I did not visit or call as often as I should have, I love you so much and you are the pillar that I can always rely on.

Curriculum Vitae

Personal data

Name: Mengyu Wang
Nationality: Chinese
Date of birth: June 20, 1983
E-mail: wangm@ethz.com

Education

2008 – present: **ETH Zurich**, Zurich, Switzerland
Laboratory for Electromagnetic Fields and Microwave Electronics
PhD., Doctor of Science, ETH Zürich
Finite element simulations and optimizations of plasmonic structures in layered media (PhD thesis)

2006 – 2008: **Zhejiang University**, Hangzhou, China
College of Information Science and Engineering
M.S. in Electronics Science and Engineering
On the application of transformation media in electromagnetics (Master thesis)

2002 – 2006: **Zhejiang University**, Hangzhou, China
College of Information Science and Engineering
B.S. in Electronics Science and Engineering
Design and simulation of RFID tag antenna (Undergraduate thesis)

1999 – 2002: **The 2nd High School**, Huhhot, China

Work and Academic Experience

- 2008 – present: **ETH Zurich**, Zurich, Switzerland
Laboratory for Electromagnetic Fields and Microwave Electronics
Research and teaching Assistant
- 2006 – 2008: **Zhejiang University**, Hangzhou, China
College of Information Science and Engineering
Research and teaching assistant